

RESEARCH ARTICLE | DECEMBER 15 2023

Quantifying uncertainty in analysis of shockless dynamic compression experiments on platinum. II. Bayesian model calibration

Justin L. Brown   ; Jean-Paul Davis  ; J. Derek Tucker  ; Gabriel Huerta  ; Kurtis W. Shuler



J. Appl. Phys. 134, 235902 (2023)

<https://doi.org/10.1063/5.0173652>



View
Online



Export
Citation

CrossMark



AIP Advances

Why Publish With Us?

 25 DAYS average time to 1st decision

 740+ DOWNLOADS average per article

 INCLUSIVE scope

[Learn More](#)

 AIP Publishing

Quantifying uncertainty in analysis of shockless dynamic compression experiments on platinum. II. Bayesian model calibration

Cite as: J. Appl. Phys. 134, 235902 (2023); doi: 10.1063/5.0173652

Submitted: 23 August 2023 · Accepted: 3 November 2023 ·

Published Online: 15 December 2023



View Online



Export Citation



CrossMark

Justin L. Brown,^{a)}  Jean-Paul Davis,  J. Derek Tucker,  Gabriel Huerta,  and Kurtis W. Shuler

AFFILIATIONS

Sandia National Laboratories, Albuquerque, New Mexico 87185, USA

^{a)}Author to whom correspondence should be addressed: jlbrown@sandia.gov

ABSTRACT

Dynamic shockless compression experiments provide the ability to explore material behavior at extreme pressures but relatively low temperatures. Typically, the data from these types of experiments are interpreted through an analytic method called Lagrangian analysis. In this work, alternative analysis methods are explored using modern statistical methods. Specifically, Bayesian model calibration is applied to a new set of platinum data shocklessly compressed to 570 GPa. Several platinum equation-of-state models are evaluated, including traditional parametric forms as well as a novel non-parametric model concept. The results are compared to those in Paper I obtained by inverse Lagrangian analysis. The comparisons suggest that Bayesian calibration is not only a viable framework for precise quantification of the compression path, but also reveals insights pertaining to trade-offs surrounding model form selection, sensitivities of the relevant experimental uncertainties, and assumptions and limitations within Lagrangian analysis. The non-parametric model method, in particular, is found to give precise unbiased results and is expected to be useful over a wide range of applications. The calibration results in estimates of the platinum principal isentrope over the full range of experimental pressures to a standard error of 1.6%, which extends the results from Paper I while maintaining the high precision required for the platinum pressure standard.

15 December 2023 15:38:29

Published under an exclusive license by AIP Publishing. <https://doi.org/10.1063/5.0173652>

I. INTRODUCTION

As highlighted in Paper I,¹ dynamic ramp compression experiments enable exploration of how a material compresses to pressures of 100 s of gigapascals with only modest increases in temperature. Advances in the analytic analysis method used to interpret the data from these experiments have enabled high-precision measurements of the room temperature pressure-density response for a variety of metals, such as copper, gold, and platinum.^{2,3} This method is broadly referred to as inverse Lagrangian analysis (ILA) here for simplicity but contains several steps to reduce the measured compression path to an isotherm.^{1–3} While ILA has been found to be suitable for these relatively simple metals, there are inherent approximations within ILA that may not make it broadly applicable for all materials. Of particular concern, path and/or time-dependent material response that can arise from a number of factors, such as loading conditions, material strength, and phase transformations, may result in systematic errors in ILA. Additionally, ILA is the only method widely accepted that is

capable of making quantitative inferences about the loading path from the velocity-time histories typically measured in ramp compression experiments. Thus, it is of interest to explore different analysis methods that operate under different approximations for cross-validation of the solutions and to build confidence in the interpretation of the experiments as the community moves to ever more complex experiments and materials.

As a test case for a new analysis method, we examine the pulsed-power driven platinum (Pt) experiments detailed in Paper I.¹ The configuration for these is, by design, conducive to computational modeling of the experimental observables. This is to say that the framework for establishing a validated computational model for the magneto-hydrodynamics describing the wave propagation within these experiments is well established.^{4–6} At a high level, this model takes inputs in the form of the material models and the experimental parameters, such as the boundary condition and material thicknesses, and outputs a simulated velocity-time history that can be directly compared to the experimental measurement.

If one assumes that everything in the computational model is well constrained except for the sample's equation of state (EOS), then it is possible to optimize on the EOS such that a best match between simulation and experiment is obtained. Indeed, the very nature of these experiments is to maximize sensitivity of the measured velocity waveforms to the EOS of interest making this is a well-posed inverse problem.

There are a plethora of optimization methods well-suited to solving our inverse problem. However, most of them are deterministic. It is relatively straightforward to define an optimization metric, such as an L2 norm, describing the difference between the experimental and simulated velocity and optimize on the EOS to give a single-valued solution. The problem with this type of deterministic approach is that there is no uncertainty quantification (UQ), and UQ is germane to these experiments and their ability to establish high-precision standards. UQ approaches generally fall into two approaches: frequentist and Bayesian. There are pros and cons of each approach, but we choose to pursue a Bayesian approach here as there are many advantages that make it attractive for our application. First, Bayesian model calibration (BMC) has uncertainty quantification embedded within the very fabric of its framework, and it is capable of incorporating every relevant source of uncertainty of interest. Second, BMC is a common approach within the physical sciences to calibrate computational models against experimental measurements. Thus, we can leverage the vast amount of work on this topic that provides the mathematical rigor justifying the quantitative inferences. We do not provide an exhaustive list of references here but refer the reader to Kennedy and O'Hagan's seminal paper on BMC⁷ and the direct adaptation of this approach to Z ramp compression experiments.^{8,9} Third, Bayesian methods can incorporate prior knowledge. It is relatively easy to make precise measurements of the sample's ambient properties, such as its initial density and bulk modulus. BMC can naturally integrate these types of additional measurements and their uncertainties into the calibration to provide important constraints and improve the overall inferences. Fourth, many BMC frameworks allow for inference of model discrepancy.^{7,10} Our computational model will never be perfect, and it contains many complexities beyond the sample material model; Bayesian methods that account for model discrepancy reflect this fact. Finally, and perhaps most importantly, BMC integrates with complex simulations and material models giving it the potential to provide a viable analysis approach in situations where ILA may break down. Referring back to the example about materials undergoing phase transformations: in one of the most well-studied of dynamic phase transformations, the $\alpha \rightarrow \epsilon$ transition in iron has been observed under ramp compression to exhibit significant dependence on loading rate in the ILA result.¹¹ It is not clear to what level time-dependence violates the approximations in ILA and the magnitude of systematic errors it induces, but BMC offers an alternative analysis pathway that may prove useful in better understanding the experiments.

The rest of the article is organized as follows. Section II details the computational model, data integration, and platinum models considered for calibration. Of particular note, the platinum EOS models considered include both fixed functional descriptions as well as a novel non-functional form, the latter of which is found to provide both high accuracy and high precision over the full range

of the measurements. Section III describes the BMC and sensitivity study methodologies along with the subsequent results and comparisons to ILA. Some advantages and disadvantages of the BMC method as it compares to ILA and general recommendations are given in the conclusions in Sec. IV.

II. TIES BETWEEN SIMULATION AND EXPERIMENT

A. Computational model

The experimental configuration, detailed in Paper I,¹ is designed to be accurately modeled through the 1D magnetohydrodynamic (MHD) simulation domain shown in Fig. 1. The platinum (Pt) sample of interest is bonded between a copper (Cu) electrode and an optically transparent [100] lithium fluoride (LiF) crystalline window. The time history of the magnetic field, which is determined through the corresponding *drive* measurements¹ (not shown) and the optimization process described elsewhere,^{1,4} acts as the boundary condition driving the left side of the electrode. The magnetic field generates a time-dependent stress wave through the Lorentz force that propagates ahead of the magnetic diffusion front, and the experiment is designed such that the stress wave will traverse through the Pt sample before the magnetic field diffuses through the electrode. The quantity measured in the experiment (through standard velocimetry techniques¹²) is the velocity of the Pt/LiF interface. This same quantity is easily tracked through the MHD simulation, which allows for direct comparisons between the experiment and simulation.

Simulations were performed using the Laslo 1D Lagrangian MHD research code,¹³ which solves the same equations and contains the same materials library as the ALEGRA multiphysics code.¹⁴ The computational domain consists of the measured Cu, Pt, and LiF thicknesses stacked together. Glue bonds, measured to be less than $4\mu\text{m}$ for all experiments, are neglected. The Lagrangian mesh consists of $1\mu\text{m}$ cell size at the driving end of the Cu and is graded linearly to $2\mu\text{m}$ at the Cu/Pt interface. The $2\mu\text{m}$ cell size is maintained through the Pt sample and is then linearly graded from 2 to $20\mu\text{m}$ between the Pt/LiF interface and the rear surface of the window. This mesh scheme provides good convergence with respect to the simulated velocity of interest while keeping the computational cost

15 December 2023 15:38:29

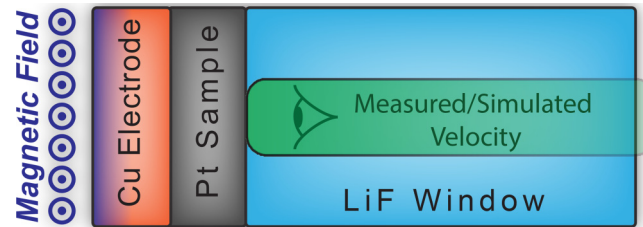


FIG. 1. Schematic of the 1D model of the experiments. A magnetic field boundary condition drives a shockless compression wave through the copper electrode and into the platinum sample. A thick optically transparent LiF window tamps the sample to keep it at an elevated pressure, while velocimetry is used to measure the interface velocity. This time-dependent velocity is the experimental observable and the metric of interest extracted from the simulations.

relatively low, which is important for the statistical methods described in Sec. III. Given the shockless nature of the simulations, artificial viscosity does not play a significant role and was set to as low a value as possible while still ensuring numerical stability. The Cu electrode and the LiF window are treated as standards with known material models, which are described in detail in Paper I.¹ Thus, the only assumed unknown in the computational model is the constitutive model for the Pt. The parameterization and subsequent calibration of the Pt response, with an emphasis on the EOS, is the primary topic of the rest of this article.

B. Experimental data and uncertainties

The measured Pt/LiF velocity data, denoted $u(t)$, are shown in Fig. 2 and consist of 11 unique profiles collected over 5 different experiments. The velocities scale with pressure such that the lowest pressure experiment (Z3112) reached ~ 170 GPa, while the highest pressure experiment (Z3064) reached ~ 570 GPa. The uncertainties associated with these velocities are given by

$$\delta u = \sqrt{(U_{\text{con}})^2 + (u U_{\text{lin}})^2}, \quad (1)$$

where U_{con} and U_{lin} depend on the diagnostic configuration¹⁵ and are summarized in Table I. Also shown are the Cu electrode thicknesses, X_{Cu} , and Pt sample thicknesses, X_{Pt} , for which uncertainties of $3\ \mu\text{m}$ are estimated for both. The LiF thicknesses of 4–6 mm were effectively infinitely thick with respect to the wave propagation so that their uncertainties are irrelevant and not included in Table I. The relative timing uncertainty between the measured and simulated Pt/LiF interface velocities is estimated to be 200 ps.¹ The uncertainty in the magnetic field boundary condition, B , is approximated to be a function of the drive velocity uncertainty and is described in detail in Appendix A, resulting in the form

$$\delta B^2 = [(0.134 + 44.35B^{-1.178})U_{\text{con}}]^2 + [(2.008 + 0.113B^{1.273})U_{\text{lin}}]^2, \quad (2)$$

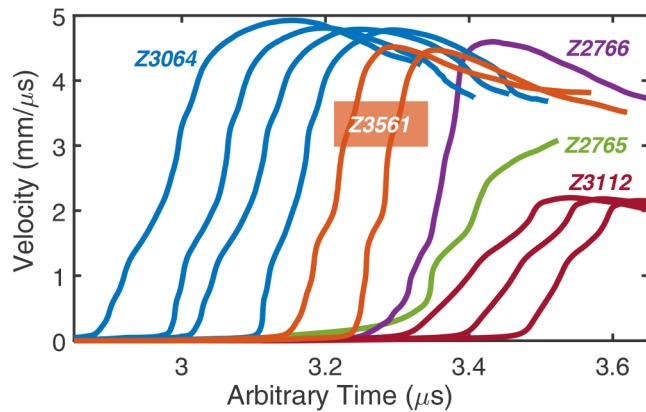


FIG. 2. Summary of the 11 velocity profiles measured in 5 different experiments. Velocities with the same color were from the same experiment and represent different sample thicknesses. Arbitrary time offsets are applied for clarity.

TABLE I. Velocity uncertainties and thicknesses from Table 1 in Paper I¹ relevant to the computational model. Not shown, the uncertainties associated with both X_{Cu} and X_{Pt} are $3\ \mu\text{m}$, the timing uncertainty Δt is 200 ps, and the uncertainty in the magnetic field boundary condition is given by Eq. (2).

Experiment	U_{con} (m/s)	U_{lin} (%)	X_{Cu} (mm)	X_{Pt} (mm)
Z2765-2	5.0	0.90	2.001	1.494
Z2766-2	4.5	0.82	2.001	1.373
Z3604-1	5.4	0.15	1.997	1.208
Z3604-2	5.4	0.15	1.997	1.404
Z3604-3	5.4	0.15	1.998	1.304
Z3604-4	5.4	0.15	1.998	1.507
Z3112-1	6.0	0.21	1.745	1.797
Z3112-2	8.7	0.49	1.746	2.000
Z3112-3	6.0	0.21	1.749	2.200
Z3561-1	6.9	0.14	1.498	1.003
Z3561-2	6.4	0.15	1.498	1.155

where the units of B are in Tesla, U_{lin} represents a unitless linear scaling term, and U_{con} relates to a constant offset in units of m/s. The coefficients in Eq. (2) effectively represent the impedance matching between Cu and LiF to estimate the magnetic pressure in the Cu as a function of the measured Pt/LiF interface velocity. Since the velocity error coefficients are well-known, this provides a convenient way to approximate the corresponding uncertainty in the boundary condition.

C. Platinum models

As described in Sec. II A, the only unknown in the computational model is assumed to be the constitutive model for the Pt sample. Within the framework of our hydrocode, this consists of an EOS model to describe the hydrodynamic response combined with a strength model to describe the deviatoric behavior. Since these experiments were not designed to be particularly sensitive to the material strength (quantified in Sec. III A), the strength model and parameter distributions in Ref. 16 are used. Briefly summarizing those results, an extremely simplistic strength model form was used,

$$Y = Y_0 (1 + A P \xi), \quad (3)$$

where P is the pressure, $\xi = (\rho_0/\rho)^{1/3}$ is the linear isotropic extension, ρ is the density, and the following independent normal distributions for the two strength parameters were obtained: $Y_0 = 0.44 \pm 0.17$ GPa and $A = 4.7 \pm 7.5$ TPa⁻¹. Of note, the peak stress for the data used to calibrate these distributions was 300 GPa so that the model will be extrapolating nearly a factor of 2 to the 570 GPa peak pressures reached by the data shown in Fig. 2. While this magnitude of an extrapolation is not ideal, the simple nature of Eq. (3) is well-behaved and honors Thomas–Fermi pressure scaling limits.¹⁷ Coupled with the relative lack of sensitivity, the extrapolation in this application is believed to be a reasonable approach in the absence of any other strength information.

As summarized in Paper I,¹ we also have information pertaining to the ambient state of the Pt. This includes the initial

15 December 2023 15:38:09

density and thermoelastic properties. Of particular relevance to the BMC, the ambient density is $\rho_0 = 21.421 \pm 0.043 \text{ g/cm}^3$, and the ambient bulk isentropic sound speed is $c_0 = 3.617 \pm 0.055 \text{ mm}/\mu\text{s}$. This leaves the remaining focus of this article on the model form and parameterization for the high-pressure compressibility.

All of the experimental data under consideration here represent shockless compression of the sample; therefore, increases in temperature are modest³ and the isentrope is the most relevant thermodynamic reference curve. As such, we approximate the EOS through the Mie–Grüneisen approximation with the principal isentrope as the reference curve. The Grüneisen parameter, Γ , is assumed to have a linear dependence on the density,

$$\Gamma = \Gamma_0 \frac{\rho}{\rho_0}, \quad (4)$$

where $\Gamma_0 = 2.64$. To enable efficient hydrocode simulations, a limited-range Sesame tabular EOS is used in place of an analytic implementation. The Sesame table is generated using the method in Ref. 5 where a constant specific heat of $c_v = 130.1 \text{ J}/(\text{kg K})$ is used to complete the thermal description. This approach and the values used are effectively identical to what is used in ILA,¹⁸ and therefore, the thermal approximations are consistent. Not shown, a perturbation of the sensitivity analysis described in Sec. III A was run to include Γ_0 and c_v with standard deviations of 30% each. This sensitivity analysis resulted in no appreciable sensitivities to these two thermal parameters; therefore, only fixed values are used herein for computational efficiency.

Three models for the reference isentrope are examined: Vinet,¹⁹ third-order Birch–Murnaghan (BM),²⁰ and a novel method, which does not have an explicit form and so it is referred to as the non-parametric (NP) model. The philosophy behind examining different model forms is to (1) ascertain if the calibrations are sensitive to a model form, (2) determine if model form errors can be identified, and (3) determine best practices for the use of BMC in future applications.

The Vinet model is represented by

$$P = 3K_0 \frac{1 - \xi}{\xi^2} e^{\frac{3}{2}(K'_0 - 1)(1 - \xi)}, \quad (5)$$

where K_0 is the ambient isentropic bulk modulus and K'_0 is its pressure derivative. The BM model contains the same three parameters (ρ_0, K_0, K'_0) but with a very different functional form,

$$P = \frac{3}{2} K_0 [\xi^{-7} - \xi^{-5}] \left\{ 1 + \frac{3}{4} (K'_0 - 4) [\xi^{-2} - 1] \right\}. \quad (6)$$

The NP model is fully motivated later in Sec. III A where there is a clear need for a model form that provides localized causality between the reference isentrope of interest and the measured velocity over the full range of the data. The idea behind this model is summarized in Fig. 3, where a series of knots are used in conjunction with a spline interpolation to provide the flexibility to produce a completely arbitrary reference curve that is not bound by a parametric model form. The space to define this reference curve is somewhat arbitrary, but the most intuitive choice would be to

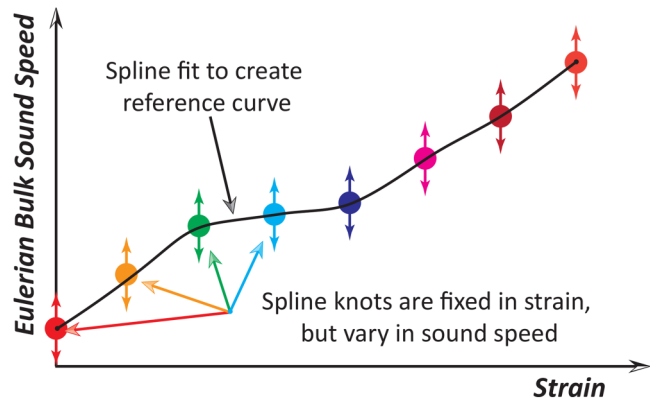


FIG. 3. The non-parametric (NP) model form consists of a series of knots at fixed pre-determined strains and variable Eulerian bulk sound speeds. Each instance of the knot magnitudes is interpolated by a spline to create an instantiation of the reference isentrope curve.

15 December 2023 15:38:29

match the BM and Vinet functional forms: pressure as a function of compression. Unfortunately, we found this form presented significant challenges in running the hydrocode simulations since small perturbations can result in large changes to $dP/d\rho$ (i.e., the sound speed squared), which caused robustness issues in getting the simulations to run to completion. Subsequently, this led to a search for spaces where the thermodynamic derivatives can be used instead. The space chosen to be ideal in this work is the Eulerian sound speed, C_E , as a function of strain. Several choices were considered, such as Lagrangian sound seed ($C_L = C_E \frac{\rho}{\rho_0}$) as a function of particle velocity, $C_L(u)$, to mimic ILA¹ and bulk modulus as a function of pressure, $K(P)$, as an intuitive choice for what is gained from these experiments: the compressibility as a function of pressure. While the results from these choices were the same to within the uncertainties in the final inferred pressure–density response, there are subtle differences in correlations between the variables that lead to differences in the uncertainties in other spaces. Calibrations with the bulk modulus ($K = \rho C_E^2$) or the Lagrangian sound speed, for example, introduce correlation with the initial density that manifests as an increase in uncertainty in these variables. Furthermore, as discussed in Ref. 1, the particle velocity is not a thermodynamic state variable, and therefore, it is avoided in this framework for clarity. This naturally leads to a desire to isolate C_E as the dependent variable, and since deformation mechanics (such as in a hydrocode) are typically expressed as a function of strain, we choose the volumetric strain as our independent variable. Using strain also has the convenience of normalizing the initial density, which makes it trivial to use a fixed grid of reference points; attempts to use a fixed grid of density points, on the other hand, created numerical difficulties in accommodating uncertainty in the initial density.

Once the knots are determined, the reference curve is given by interpolation. We found that the nature of the interpolating function is an important consideration. As will be discussed in Sec. III B, the number of knots plays into a bias–variance tradeoff

where a greater number of knots allows for greater fidelity in the mean at the expense of increased correlation between the knots and, thus, greater variance in posterior probability distributions. Thus, it is desirable to have an interpolating function that will accurately describe the curve of interest with the minimum number of knots. In our testing of a variety of interpolation methods, including the linear, cubic, and piecewise cubic hermite interpolating polynomial (PCHIP),²¹ we found that the PCHIP method could most accurately interpolate over the known response from ILA using the smallest number of points. The differences between the methods only manifest for sparse numbers of points, but in those cases, the lack of continuity in the derivatives with the linear interpolant and the overshoots characteristic of cubic splines becomes apparent. As such, the PCHIP method was used to interpolate on each instantiation of the knots to form the isentrope reference curve for all results presented herein. However, this was not an exhaustive search of all interpolating methods available in the literature, and future work is planned for a more comprehensive examination of options.

III. STATISTICAL ANALYSES

Two statistical methods are used to interpret the data, the complete details of which are summarized elsewhere.^{8,9} First, global variance-based sensitivity analysis²² is a way to examine how much an uncertain parameter in the simulation contributes to the uncertainty in our metric of interest: the Pt/LiF interface velocity. This is particularly useful for understanding how much each of the parameters in the models described in Sec. II C influences specific regions of the velocity profile. Conversely, in solutions of an inverse problem through methods, such as calibration, the sensitivity analysis illustrates which regions of the velocity profile will constrain the calibration of which parameters.

The second statistical method and primary focus of this article is Bayesian model calibration (BMC). BMC results in probability distributions and correlations for each of the uncertain variables in the simulation. The distributions for the Pt model parameters can then be propagated through their respective models to determine curves of interest, such as pressure-strain, with well quantified uncertainties. The primary goal of this work is to understand the viability, advantages and disadvantages, and best practices associated with using BMC to infer the Pt material properties over the range of conditions sampled in the experiments.

BMC is a well established method within the physical sciences⁷ which has been adapted specifically to the types of Z experiments of interest here.^{8,9} The primary challenge with calibrations over velocimetry-based ramp compression data is the functional nature of the velocity-time histories. The original adaptation in Ref. 8 dealt with this functional data issue by treating each point along the velocity-time waveform as independent and then scaling the likelihood function to account for the autocorrelation between the points. As with the original work on tantalum⁸ we found this scaling approach worked well for the Pt calibrations over the parametric models. However, applying this method to the non-parametric model was found to exhibit significant overfitting and subsequent under-estimation of the errors. As such, the improved framework of Francom *et al.*⁹ was used for all calibrations shown

herein. This newer framework is fully functional throughout, meaning it incorporates the entire velocity-time history into the surrogate model and the likelihood function without approximation. This also means that the surrogate model error is quantified and incorporated into the analysis, which was not possible in the original adaptation due to computational constraints.⁸ Additionally, a novel procedure is used to align the simulations to the data not only in amplitude (velocity) but also in phase (time), which can provide dramatic improvements for data that include shocks.⁹ We find this improved framework does not appreciably alter the BMC results for the parametric models,⁹ but dramatically improves the quality of the non-parametric calibrations. Moreover, the emulators that are generated from the training data can be used directly for sensitivity studies,²³ meaning the posterior distributions from the BMC can be post-processed through the sensitivity analysis for even better consistency and further insights into the calibrations.

A. Global sensitivity analysis

Variance-based global sensitivity analysis²² was performed for each experiment and for each Pt model of interest using the method described by Francom *et al.*²³ The method is intrinsically tied to the calibrations discussed later in Sec. III B but is discussed first as it provides useful insights into the differences between the parametric and non-parametric models. In practice, this sensitivity analysis effectively acts as a post-processing step to the BMC as the posterior distributions are implemented directly in a closed form solution to generate the Sobol sensitivity indices.²³ This provides perfect continuity between the BMC and sensitivity studies such that the sensitivity analysis accurately reflects the probability distributions and correlations of interest. The downside of this method is that it utilizes complex posteriors so that it is difficult to succinctly summarize all of the distributions used in the analysis. The priors for these distributions are summarized in Tables I and II, while a subset of the posteriors are summarized in the BMC results in Table III and Figs. 10 and 11. Further details, such as summaries of all of the posterior distributions, are not provided since the sensitivity analysis is ultimately only used for qualitative insights. Furthermore, we find that while the sensitivities vary with each experiment, they are reasonably bound by the lowest pressure (Z3112-1) and the highest pressure (Z3064-4) experiments. As such, only the results from these two experiments are given in the

15 December 2023 15:38:29

TABLE II. Prior distributions for the Pt model parameters used to generate the training data. BMC proceeds by taking the range of the sampled training data as a uniform prior.

Initial density	$\rho_0 = \mathcal{N}(21.42, 0.04) \text{ g/cm}^3$	
Strength ¹⁶	$Y_0 = \mathcal{N}(0.44, 0.17) \text{ GPa}$	$A = \mathcal{N}(47, 8) \text{ TPa}^{-1}$
EOS—Vinet	$K_0 = \mathcal{N}(260, 10) \text{ GPa}$	$K'_0 = \mathcal{N}(5.8, 0.3)$
EOS—BM	$K_0 = \mathcal{N}(279, 10) \text{ GPa}$	$K'_0 = \mathcal{N}(5.1, 0.3)$
EOS—NP ^a	$\mathcal{N}(\text{Sesame 3732 isentrope}, 15\% \text{ knot magnitude})$	

^aFixed strains are five equally spaced points on the interval [0,0.415].

TABLE III. BMC posterior distributions for the parametric models. The distributions are well approximated by a multivariate normal distribution.

Model	ρ_0 (g/cm ³)	K_0 (GPa)	K'_0	Corr(K_0 , K'_0)
Vinet	21.56±10.1	270.96±1.75	5.75±0.05	-0.47
BM	21.25±0.08	268.83±1.92	5.42±0.08	0.27

main text for brevity. However, a comprehensive set of results can be found in Figs. 13–15 of Appendix B.

1. Parametric models

The distributions of the majority of the uncertain parameters across the sensitivity studies were similar, with the obvious exception of the Pt model form. For the parametric models, Vinet and BM, there are only three physical parameters of interest: ρ_0 , K_0 , and K'_0 . The results for the Vinet model are shown in Fig. 4. The BM model results are not shown here because they are extremely similar and exhibit the same trends of interest; again, we refer the interested reader to Appendix B for the complete set of results.

Figure 4 summarizes the results from the Vinet sensitivity analysis for the lowest pressure (Z3112-1) and the highest pressure (Z3064-4) experiments. The time-dependent proportion variation

represents the cumulative first-order sensitivity index such that the unexplained variance, labeled *other*, represents the amount of variance due to correlations. The strong sensitivities of the Vinet parameters of interest, ρ_0 , K_0 , and, K'_0 , coupled with the relatively low sensitivities of the other experimental and material model (strength) uncertainties suggest that they are highly identifiable, and therefore, their calibration will be to high confidence. The time-dependent nature of the Vinet parameters' proportion variance is largely intuitive, although slightly different between the two experiments. In Z3112, ρ_0 is relatively constant but is not the biggest lever arm, while K_0 dominates at lower velocities and K'_0 is the primary sensitivity at higher pressures. This is exactly what is expected based on the nature of the parametric models since ρ_0 permeates the functional form in Eq. (5), while K_0 dictates the ambient sound speed and K'_0 is the lone term associated with the higher pressure states. Z3064 exhibits similar trends but contains lower overall sensitivities to K_0 and K'_0 , which is consistent with expectations since at higher pressures, the increased sound speed results in decreased transit time (i.e., less sensitivity). There is also an increase in ρ_0 coupled with a re-emergence of K_0 near 3.35 μs that is associated with the reflection of the low-pressure portion of the wave backward off the window interface interacting with the electrode interface (i.e., reverberation). Usually, reverberation violates Lagrangian analysis, and so this is the time at which the analysis has traditionally been terminated. The present ILA contains a

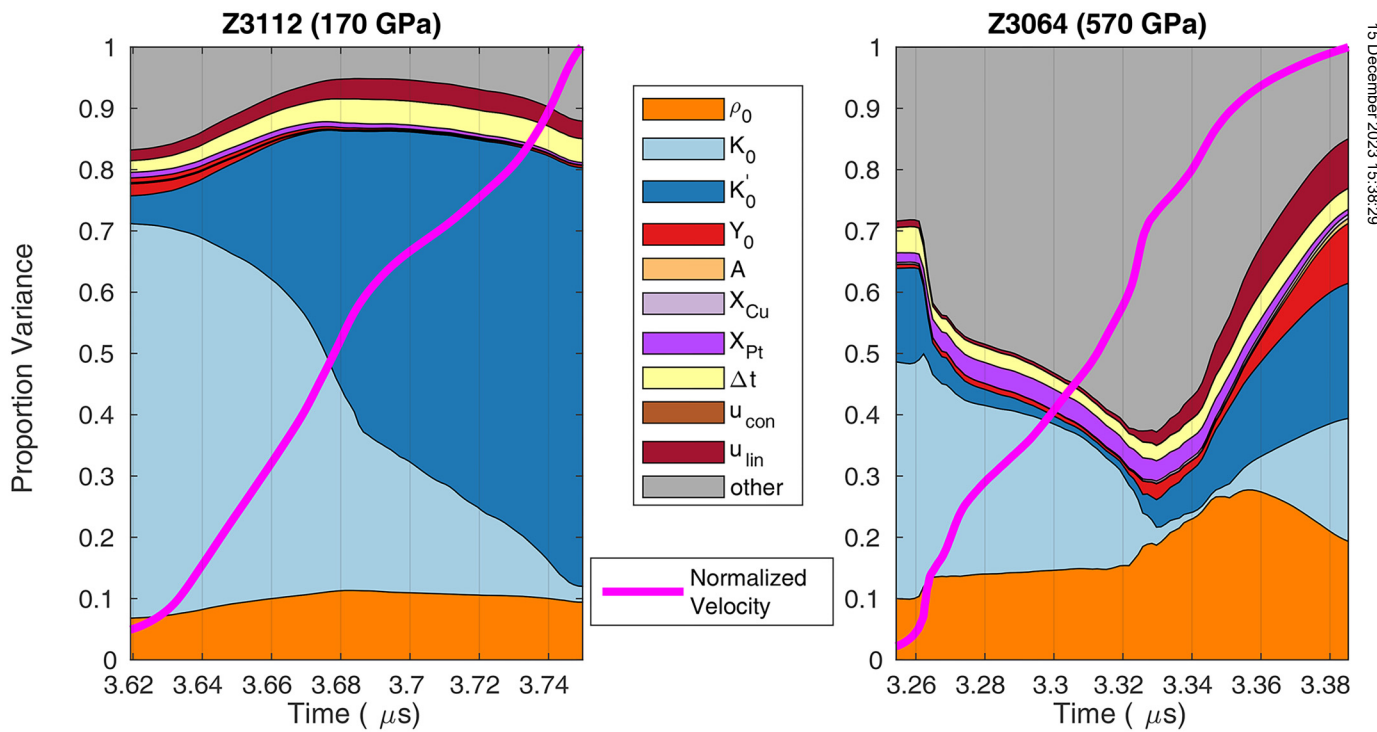


FIG. 4. Sensitivity analysis for the lowest pressure (Z3112-1) and the highest pressure (Z3064-4) experiments using the Vinet EOS and the posterior distributions from the corresponding BMC in Sec. III B. The proportion variance represents the cumulative first-order sensitivity index, and each parameter and experiment has a time-dependent structure related to the respective velocity profiles shown as the magenta curves.

new post-reverberation correction that should extend the analysis range, but a non-single-valued response due to localized regions of release from strength effects cause a more nuanced issue that also results in cutting off the analysis prior to peak.¹ This sensitivity analysis demonstrates that there remains good sensitivity to K'_0 all the way to the peak velocity. Since reverberation and strength effects are wave interactions inherently modeled within the hydrocode simulations, the calibrations are able to maintain sensitivity through the entirety of the measurement. This is the reason the BMC results shown later reach higher pressure than ILA. A less intuitive result from Fig. 4 is the interplay between the relative sensitivities between the experiments. In the lower pressure experiment, the K_0 and K'_0 sensitivities crossover roughly halfway up the velocity profile. Curiously, this crossover occurs roughly 3/4 up the velocity profile for the higher pressure experiment. In other words, the relative amount of information learned is not only different between each experiment, but the parameter inferences will also be influenced by different velocity/pressure regimes. The low pressure experiment, for example, demonstrates a very high proportion variance to K'_0 , while the higher pressure experiment does not. Thus, the inference of K'_0 is likely based primarily on the low-pressure data, which means that the parametric models are largely extrapolating to the highest velocities rather than being highly constrained by them. However, since the likelihoods (difference between experiment and simulation) are summed to dictate the most probable solutions, this is a rather complex interaction and it is difficult to fully quantify.

The rest of the uncertain parameters in Fig. 4 do not reveal any surprises. The strength parameters, Y_0 and A , are relatively minor and manifest as contributions primarily at early and late times associated with the elastic precursor and elastic effects near peak due to loading reversal, respectively. This is consistent with the understanding of these experiments where the gross effect of strength on most of the velocity profile is small (i.e., strength has a slight effect on the wave speed)¹ until near the velocity peak where the load reversal results in elastic effects, which introduce strong sensitivity to strength. This is why the ramp-release experiments described in Ref. 16 were able to make an inference on the strength parameters. While the sensitivities here are not large enough to make both strength parameters highly identifiable, they are still present as a relevant effect, particularly in the higher pressure experiments. This is congruent with the analysis in Paper I where strength is a relatively small but important correction in reducing the measurements to the isentrope of interest.¹ The magnetic field scaling term U_{lin} , timing Δt , electrode thickness X_{Cu} , and sample thickness X_{Pt} are found to be small but relevant experimental uncertainties, which is expected based on the conventional interpretation of these experiments.¹ Similar to the strength terms, the experimental errors do not overwhelm the sensitivities of the Vinet parameters of interest, but they are of sufficient magnitude that their inclusion is warranted to get a proper estimate of the uncertainties in the Bayesian inference. The remaining parameter associated with the magnetic field offset, U_{con} , does not manifest as measurable sensitivity. This term represents a relatively small offset in the magnitude of the magnetic field that is expected to impact only the lower velocity regions of the calibration; it appears to be dwarfed by the other uncertainties in these experiments, which

suggests that the single scaling term used in previous studies^{8,9} is a good approximation.

2. Non-parametric model

The parametric sensitivity study in Fig. 4 motivates the need to examine a non-parametric form. Since the high-pressure compressibility parameters in the parametric forms (namely, K'_0) span broad regions of the velocity profile, the BMC inference will only globally fit the data. Furthermore, as described in Sec. III A 1, an additional complication is that it is not clear when calibrating over multiple experiments/pressure regimes how the parametric model is being constrained; the results in Fig. 4 suggest that the model is primarily being fit to the lower pressure regions of the measurements. The consequence is that the highest velocity regions of the calibrated fit represent an extrapolation of the model form from its fit to the lower velocity region. Given some of these potential deficiencies in calibrating over the parametric models, it is desirable to examine the characteristics of alternative model forms. An additional motivation is the need to examine materials which undergo phase transformations. This is beyond the scope of the Pt application here, but of broader interest to the community. While it may be possible to combine multiple single phase parametric models together through a phase transformation kinetics model to capture multi-phase behavior, there is interest in examining a simple model with the potential to handle the non-monotonic wave speed response typically observed in materials with phase transformations.^{11,25} Toward this end, we explore the use of the NP model described in Sec. II C to form a completely generalized reference curve that can localize sensitivities to specific regions of the velocity profiles. The NP sensitivity analysis results shown in Fig. 5 suggest that this has the desired behavior.

The sensitivity analysis in Fig. 5 is a reflection of the BMC results shown later in Fig. 10. There are five equally spaced knot locations, labeled c_1 – c_5 across the strain space between 0 and 0.415 where the maximum value of 0.415 was determined *a priori* through simulations of the highest pressure experiment. The results indicate the desired feature of this model: each knot has sensitivity localized over specific ranges of velocity. The low-pressure experiment Z3112, for example, has a known peak stress of 170 GPa, which means that it should not be sensitive to knots 4 or 5. Indeed, Fig. 5 exhibits strong sensitivity to the first three knots and, in particular, c_3 , which correlates to the highest regions of the velocity profile. The higher pressure experiment Z3064 exhibits similar qualitative trends but adds strong sensitivities to the highest pressure knots c_4 and c_5 . Of note is the respective sensitivity of the knots between the different experiments, particularly c_3 . Since the material model parameters are assumed the same across all experiments, the same variance for the knots is being propagated through each experiment's sensitivity analysis. In other words, c_3 is being highly constrained by the lower pressure experiment and very little by the high-pressure experiment, much like K'_0 in the parametric study. Conversely, the high-pressure knots, c_4 and c_5 , are being constrained entirely by the high pressure experiments. Thus, unlike the parametric models, there is a guarantee that the extracted high-pressure response and the corresponding errors are being properly inferred and not extrapolated from a lower pressure inference. The

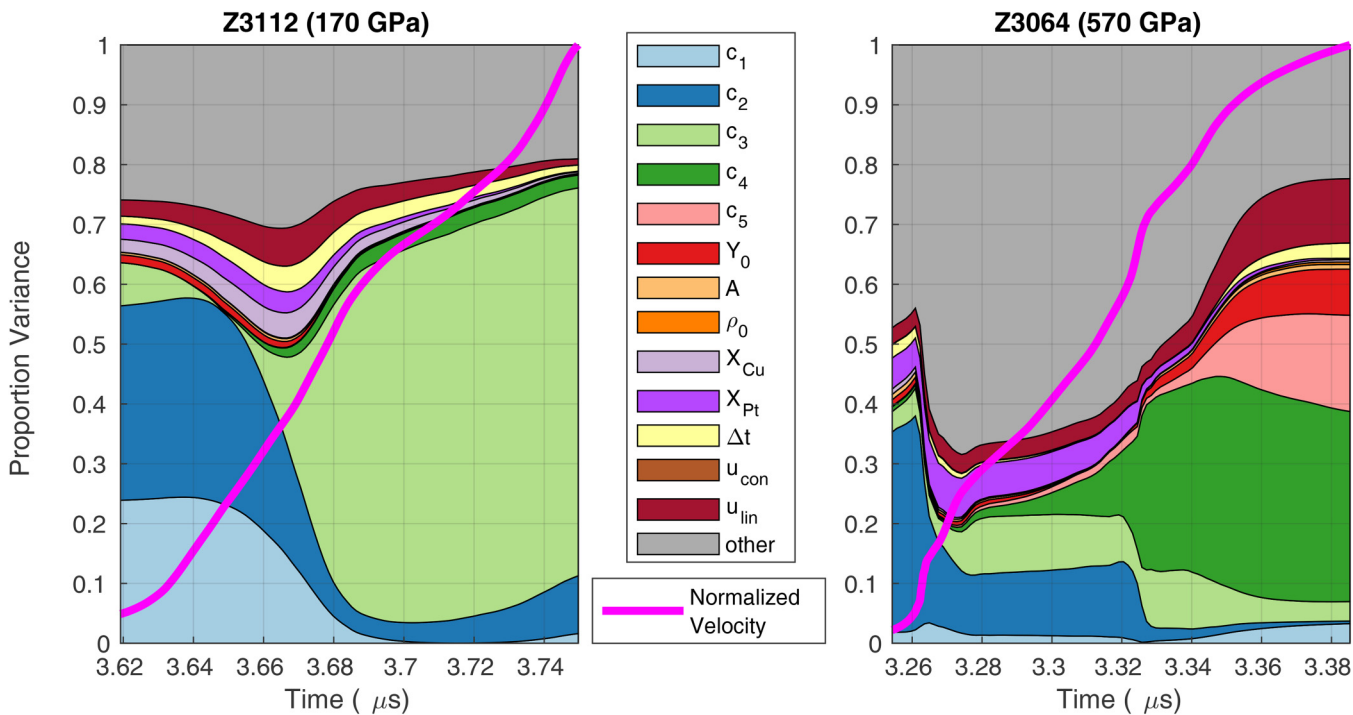


FIG. 5. Sensitivity analysis for the lowest pressure (Z3112-1) and the highest pressure (Z3064-4) experiments using the non-parametric (NP) model form and the posterior distributions from the corresponding BMC in Sec. III B. The knot locations are shown in Fig. 10 where c_1 and c_5 correspond to the minimum (strain = 0) and maximum (strain = 0.415) of the axis. The proportion variance represents the first-order sensitivity index, and each parameter and experiment has a time-dependent structure related to the respective velocity profiles shown as the magenta curves.

15 December 2023 15:38:29

final feature of note in Fig. 5 is the weak sensitivity to the initial density, ρ_0 . This lack of sensitivity contrasts with what is observed with the parametric models, but, as discussed in Sec. II C, this is the intended behavior and a direct consequence of the construction of the NP model form. There are choices of calibration spaces (such as a pressure-density reference curve) that would result in strong initial density sensitivity, but it is our interpretation that this is not appropriate for data of this type since the experiments ultimately measure wave speed and not stress or density. However, this choice results in poor identifiability in ρ_0 for this model and is a consideration for the BMC results discussed later in Sec. III B.

As with the parametric model, the experimental uncertainties in Table I are inferred individually for each experiment, and therefore, these get balanced against the rest of the uncertain variables along with the velocity error. As a result, these relative uncertainties are experiment dependent, and therefore, there is some experiment-to-experiment variability in their inference (see Appendix B). However, they exhibit the expected trends⁸ and are consistent with the parametric sensitivity analysis in Fig. 4 in the sense that the experimental uncertainties have an effect on the overall errors but do not dominate the measurement.

The NP sensitivity analysis in Fig. 5 also reveals some of the challenges associated with using the NP model. The calibration results are intrinsically tied to the choice of the number of knots

and their locations. The smooth nature of the sensitivity of the transitions reveals the smooth interpolation between the knots such that there is a correlation between them. This is particularly evident in c_1 and c_2 , where at the lowest pressures, one would expect c_1 to completely dominate. Instead, the interpolation creates an interaction between c_1 and c_2 , and this correlation introduces strong sensitivity of c_2 at the lowest pressures. However, the analysis also reveals that there is still good identifiability of each of these knots, and therefore, their inference is still expected to be accurate. This is justified by the strong sensitivities relative to the amount of the *other* variance represented by the gray region in Fig. 5. This *other* variance represents the higher order interactions between the variables and is a measure of how difficult (how uncertain) it is to uniquely infer each parameter. In the lower pressure experiments, the *other* variance is sufficiently low that correlations will not add a significant amount of uncertainty to the posterior distributions. Conversely, knots c_1 , c_2 , and c_3 in the higher pressure experiments see reduced sensitivities with a significant amount of *other* variance. If the BMC were to be conducted on a per-experiment basis, this would result in appreciable identifiability issues in these lower pressure knots and inflated variance in their posterior distributions. Fortunately, in our application, the calibration over all of the experiments will utilize the advantages of the lower pressure experiments such that good inferences of the low pressure knots are still

obtained. The high-pressure experiments then reveal good sensitivity (low *other* variance) to knots c_4 and c_5 such that good inferences are obtained across the entire range of knots. This reveals the advantages of calibrating over a diverse data set spanning multiple pressure regimes. We are in an advantageous position with the Pt data of interest here, but care should be taken in other applications where the data may be more sparse.

The preceding discussion alludes to the dependence of the solution on the choice of knot locations. In our testing, we found that this design decision results in a bias-variance trade-off. With more knots, it is possible to obtain greater flexibility in the curve but at the cost of increased correlation and, thus, greater variance. Our approach here was to start with a large number of knots (ten) to obtain a curve with low bias but high variance. The mean of this result was then re-fitted with a lower number of knots. We found that fitting between five and ten knots did not appreciably change the quality of the fit, while using only four knots began to introduce significant residuals. Thus, we settled on five knots as the optimum to maintain low bias while minimizing correlations. We note that everything in this process utilized a uniform knot spacing over the fixed strain interval of [0,0.415]. An opportunity for future work is to incorporate a method that optimizes the number of knots and their locations for maximum effectiveness.

B. Bayesian model calibration

Bayesian model calibration (BMC) was performed using the methodology in Francom *et al.*,⁹ known as elastic BMC, to estimate the posterior probability distributions for all of the uncertain variables incorporated into the computational model. Of particular interest are the Pt EOS parameters: ρ_0 , K_0 , and K'_0 for the Vinet and BM parametric models and the knot magnitudes using the NP approach.

Elastic BMC is an extension of the Bayesian model calibration approach introduced in Ref. 7. Several different approaches have been proposed to extend BMC to more explicitly accommodate functional responses,^{8,26–28} but the most common use a basis decomposition of the functional responses and then calibrate in the basis coefficient space. Using this technique, the responses are modeled as

$$z(t, \mathbf{x}_i) = y(t, \mathbf{x}_i, \boldsymbol{\theta}) + \boldsymbol{\varepsilon}_i(t, \mathbf{x}_i), \quad \boldsymbol{\varepsilon}(t, \mathbf{x}_i) \sim \mathcal{N}(\mathbf{0}, \boldsymbol{\sigma}_{\varepsilon}^2), \quad (7)$$

where $z(t, \mathbf{x}_i)$ denotes an experimental measurement from the i th experiment, $y(t, \mathbf{x}_i, \boldsymbol{\theta})$ denotes a simulated response under the same experimental conditions \mathbf{x}_i , and t parameterizes the functional responses (e.g., time). $\boldsymbol{\varepsilon}_i(t, \mathbf{x}_i)$ denotes the observation error, and $\boldsymbol{\theta}$ is a vector of the model parameters (e.g., ρ_0 , K_0 , and K'_0).

When fitting the model, t is typically discretized onto a grid, and when the calculation of y is computationally expensive, an emulator or surrogate model is used for more rapid evaluation at any parameter combination. We use the Bayesian adaptive spline surfaces (BASS)²³ approach as a surrogate for y , which uses a principal component basis to construct the surrogate.

Inference on the parameters is performed via Bayes' rule, incorporating the prior information about $\boldsymbol{\theta}$, the experimental responses, and the simulated responses together to form a posterior probability distribution over $\boldsymbol{\theta}$. Because the denominator in Bayes'

rule contains a high dimensional integral over $\boldsymbol{\theta}$, which is typically intractable, the most common approach in Bayesian estimation is to take samples from the posterior distribution of $\boldsymbol{\theta}$ via Markov Chain Monte Carlo (MCMC), rather than calculate the Bayes' formula directly. In statistics, MCMC defines a set of algorithms to generate random numbers from a probability distribution that is intractable analytically. MCMC methods are iterative and tailored to construct a Markov chain whose stationary distribution is the probability distribution of interest. As more iterations are performed, the distribution of the samples from MCMC will resemble more the distribution of interest. In Bayesian statistics, this target distribution is the posterior distribution. MCMC is also the approach used to estimate the BASS surrogate and account for surrogate uncertainty.

Although this model can be applied without modification to the dynamic ramp compression experiments, we have found that estimation can be improved by treating response variability in the phase space (x axis, time) and amplitude space (y axis, velocity) separately. By applying a specific transformation to the experimental and simulated responses, it is possible to construct a proper distance metric between $z(t, \mathbf{x}_i)$ and $y(t, \mathbf{x}_i, \boldsymbol{\theta})$ through elastic functional data analysis.^{29,30} This metric allows for the estimation of a warping function $\gamma_{y \rightarrow z}(t) : [0, 1] \rightarrow [0, 1]$ that aligns the $y(t, \mathbf{x}_i, \boldsymbol{\theta})$ to $z(t, \mathbf{x}_i)$ in the phase space. Using this procedure, a functional response is decomposed into two new functions: A transformed, temporally aligned function and its corresponding warping function.

The model in Eq. (7) is then applied to both the aligned functions and the warping functions. This procedure reduces the discrepancy between $z(t, \mathbf{x}_i)$ and $y(t, \mathbf{x}_i, \boldsymbol{\theta})$, as the Bayesian calibration procedure in Eq. (7) without elastic alignment does not explicitly handle phase (temporal) variability. Following calibration, the warping functions' inverses can be applied to the aligned functions to produce samples in the original data space. We have found that by using this procedure to reduce modeling error, we are able to obtain superior inferences about material compressibility. We refer interested readers to Refs. 7, 9, and 28 for more details about Bayesian calibration and the elastic BMC procedure, and to Ref. 31 for more details about general Bayesian modeling and MCMC.

The elastic BMC method can be summarized as containing the following steps:

1. Use Latin hypercube (Monte Carlo) sampling over the prior distributions to determine inputs to the hydrocode simulations to obtain high-fidelity computational model training data.
2. Align training data to experiment to separate out phase (time) and amplitude (velocity) variability.
3. Use aligned training data to build surrogate models using BASS emulators over both phase and amplitude.
4. Define likelihood based on the difference between simulated and measured velocities in the phase and amplitude space.
5. Estimate posterior distributions of the uncertain parameters using MCMC sampling.

The distributions used to train the emulator are summarized in Tables I and II. The normal distributions for the BM and Vinet models are values reported in Fratanduono *et al.*³ with the standard

deviations increased 100-fold to provide full coverage of the data and so as not to bias the posteriors. The NP training points are sampled from a normal distribution given by a mean of the principal isentrope from the Sesame 3732 EOS (discretized to 5 equally spaced points over the strain interval of [0,0.415]) and the standard deviation of 15% of the Eulerian sound speed. The rest of the experimental uncertainties in Table I are well defined based on *a priori* characterization of various aspects of the experiments. After sampling across these distributions, running the corresponding hydrocode simulations, and training the emulators, MCMC sampling is performed on the surrogate with non-informative uniform priors standardized over the range of the training data. The philosophy here is to provide the highest fidelity emulator possible by sampling over a higher density of points where the priors dictate, but then to use non-informative priors within the posterior sampling so as to provide a solution mainly informed by the training data. This is particularly relevant for the choice of distributions in Table II. For example, the NP sampling distribution is centered around the Sesame 3732³² isentrope and was known *a priori* to be a close solution. Thus, good sampling is obtained for building a low error emulator, but the actual inferences use uniform distributions and so the final BMC results are not at all biased by the reference Sesame EOS. The trade-off to using non-informative priors is that we are not taking advantage of the ability of Bayesian methods to incorporate prior knowledge, and therefore, the calibrations may be overly conservative. Referring again to the treatment of the NP priors, it is entirely possible to implement a strong prior model for the reference curve, but this introduces the usual trade-offs with these types of Bayesian methods. If one were to use the ILA result as *a priori*, for example, the BMC would contain lower uncertainties at the risk of injecting error from the ILA into the calibration. Within the present framework of using independent non-informative priors, the results are believed to be conservative in their uncertainty estimates but free from quantifiable bias, which is deemed acceptable for this stage of the work.

To build the training data, a rough rule-of-thumb of 1000 samples per variable was used, resulting in a total of 10 000 simulations for the parametric models and 13 000 for the NP form. For each simulated velocity, the time history was discretized into 100 evenly spaced points in time between velocities of 100 m/s and 95% of the peak. The velocity ranges were chosen based on the sensitivity analysis in Sec. III A to maximize sensitivity to the EOS and minimize sensitivity to the regions sensitive to strength. As in previous studies,⁸ the number of training simulations and velocity points were evaluated for convergence with respect to the final posterior distributions of interest, and the values used here represent good numerical convergence while minimizing computational expense. Bayesian inference was run using the numerical method described in Francom *et al.*⁹ The Markov chains were run using modern adaptive techniques, and conventional criteria were used to evaluate mixing and ensure convergence to the proper posterior distributions.

The predictions resulting from the BMC for each model form for the highest pressure experiment, Z3064, are shown in Fig. 6. The plots show the BMC 95% prediction interval as they compare with the measured velocities and arbitrary timeshifts are introduced for clarity. The lower pressure results are not shown for brevity.

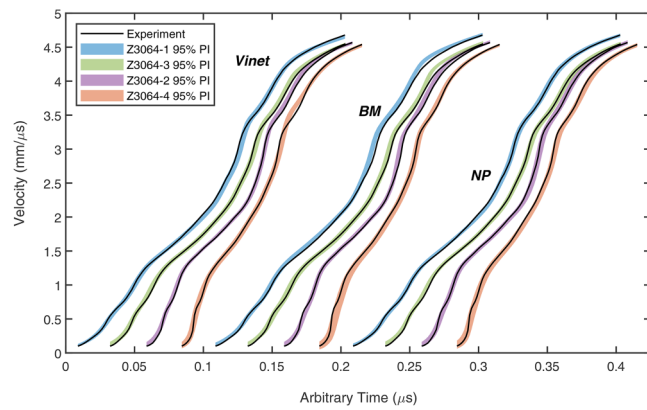


FIG. 6. BMC 95% prediction intervals (PIs) compared to the experimental data for the highest pressure experiment (Z3064) for each of the platinum models with arbitrary timeshifts introduced for clarity. The parametric Vinet and BM models exhibit regions at a high velocity that do not cover the experimental data, which is suggestive of a model form error.

15 December 2023 15:38:29

because they exhibit identical features. All of the models illustrate perfect coverage of the velocity data up to ~ 3.5 km/s, suggesting that the calibrations adequately represent the data over this range. However, close inspection of the higher velocities above 3.5 km/s for the Vinet and BM results reveals regions in some of the velocity profiles outside of the predictive interval, which is suggestive of a model form error. Reiterating the results from the sensitivity analysis in Fig. 4 and the discussion in Sec. III A 1, it is believed that the calibration of K'_0 is being driven by the lower pressure regions where more data exist and there is better sensitivity to this parameter. Thus, it is expected that the Vinet and BM models are primarily an extrapolation in these higher velocity regimes, which for some of the curves results in a poor prediction. The NP model, on the other hand, exhibits full coverage over the entire range of the data, which is the desired behavior based on how this model is constructed and the full range of sensitivities that are obtained. A final point in Fig. 6 is that the size (uncertainty) of the predictive intervals is roughly consistent across the different models. This suggests the NP model form and the choice of knot locations is not introducing significant additional variance.

The posterior distributions for the physical parameters of interest from each BMC are summarized in Figs. 7–9. These so-called *pair plots* show the marginal 1D distributions along the diagonal, kernel density estimates (KDE) of the 2D distributions along the lower diagonals, and the points from the MCMC chains colored by the log likelihood in the upper diagonals. In both sets of the off-diagonal plots, the heat maps correspond to solution pairs with high likelihood and the oblong distributions for most parameter pairs indicate high degrees of correlation. Since the priors used were non-informative uniform distributions normalized over the range of the training data, the multivariate Gaussian-like distributions that are obtained indicate that there is a strong degree of learning associated with these parameters and so they are being well constrained through the calibration; this is not surprising

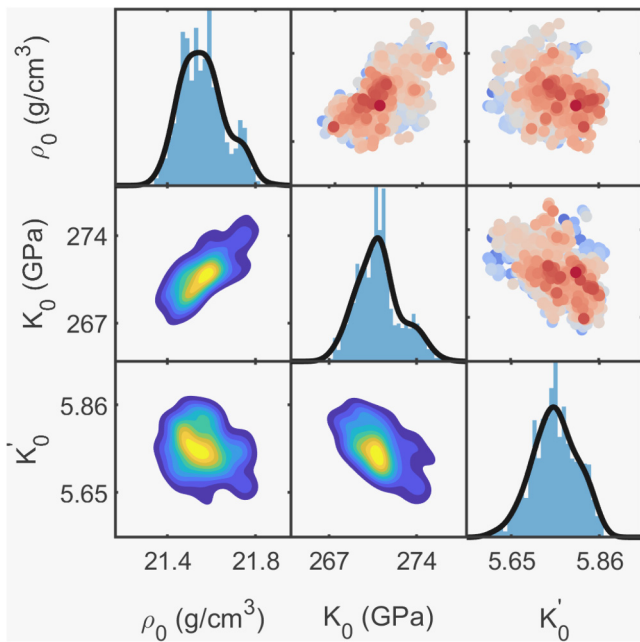


FIG. 7. Pair plot for BMC using the Vinet parametric model. The diagonals contain histograms of the 1D posterior distributions overlaid with a KDE of the distribution. The off-diagonal plots are the 2D marginal distributions and are represented by a KDE on the lower diagonals and points directly from the MCMC chain colored by the log likelihood on the upper diagonals. The axis ticks correspond to $\pm 2\sigma$ values.

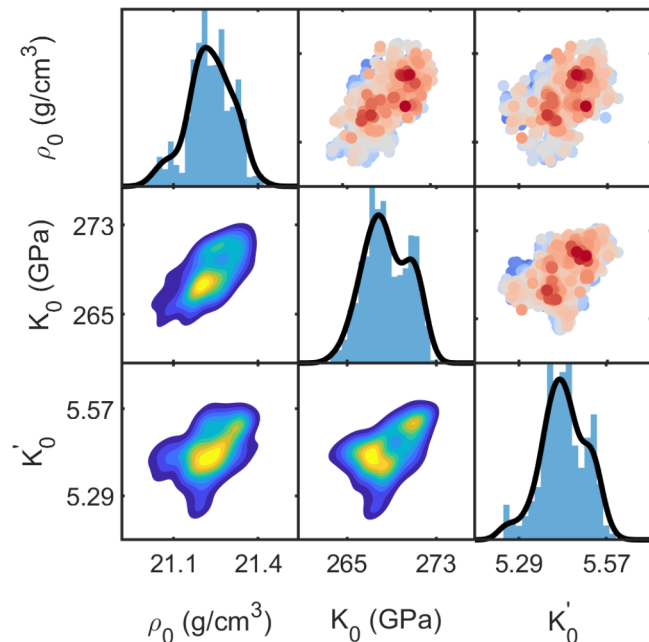


FIG. 8. Pair plot for BMC using the Birch–Murnaghan parametric model. The diagonals contain histograms of the 1D posterior distributions overlaid with a KDE of the distribution. The off-diagonal plots are the 2D marginal distributions and are represented by a KDE on the lower diagonals and points directly from the MCMC chain colored by the log likelihood on the upper diagonals. The axis ticks correspond to $\pm 2\sigma$ values.

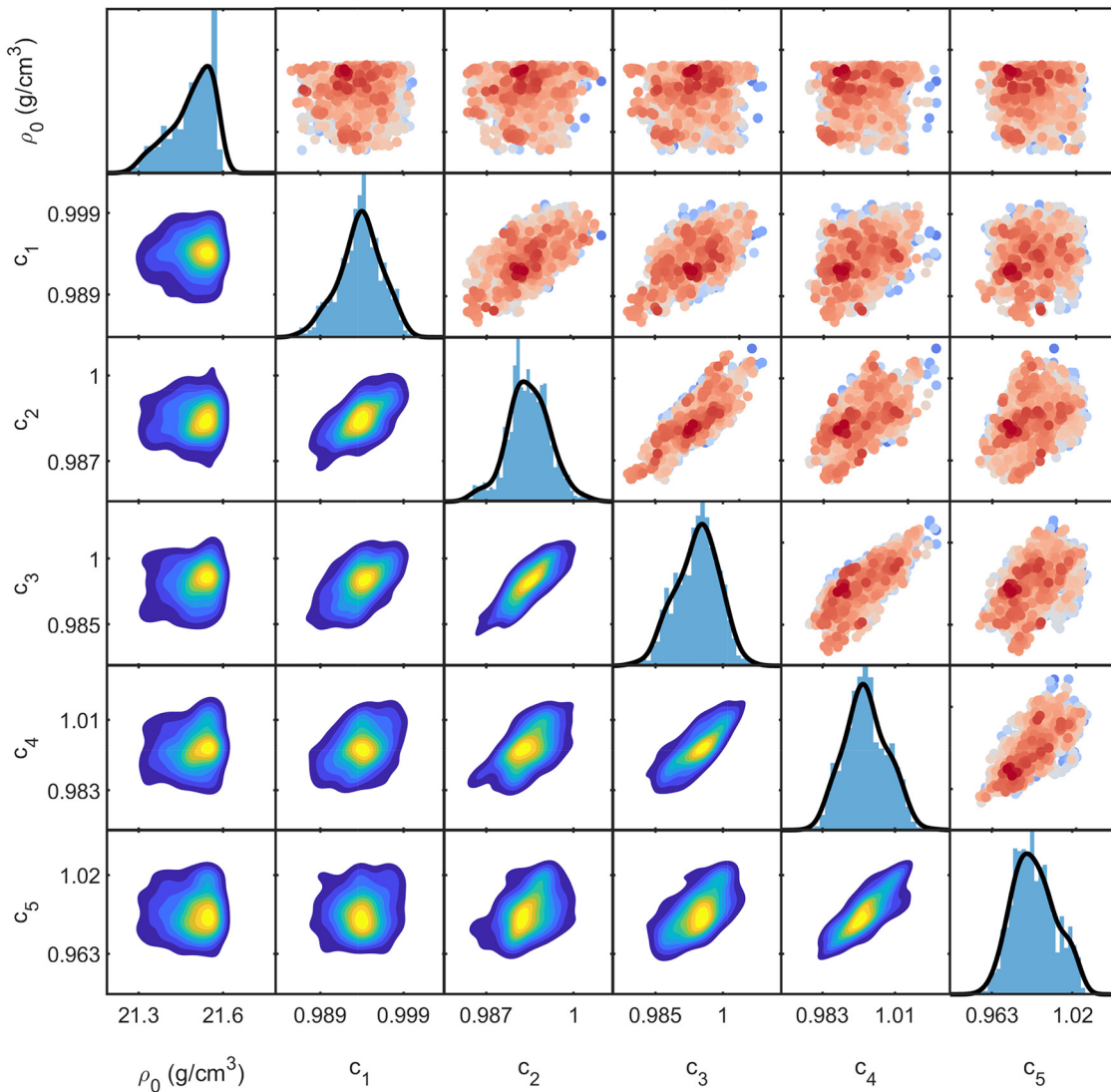
15 December 2023 15:38:29

given the results from the sensitivity analysis in Sec. III A. While the posterior distributions are not perfectly Gaussian, they are reasonably well approximated by the metrics associated with a normal distribution, the results of which are summarized for the Vinet and BM models in Table III to facilitate easy reproductions of the results. It is less useful to tabulate the NP results as, by definition, these points must be combined with the baseline amplitudes and PCHIP interpolation to form the reference curve. Instead, the distributions are propagated to curves in the two thermodynamic calibration spaces: Eulerian sound speed as a function of strain in Fig. 10 and pressure as a function of strain in Fig. 11.

There are several interesting features in the parametric BMC results in Figs. 7 and 8 and Table III. Most obviously, there are significant differences between these parameters, which have a well defined physical interpretation. As in other works on Pt,^{1,3} the pressure derivative of the bulk modulus for the different models contains differences well outside of their reported errors. This discrepancy suggests that one or both of the model forms is not accurately representing the meaning of this parameter at these extreme pressures, and so, it may be more appropriate to interpret the parameters in Table III as empirical fitting coefficients rather than physical parameters. This is corroborated by the posterior of the initial density from the BM calibration, which is on the lower end of what is plausible. The sensitivity of ρ_0 in Fig. 4 and strong correlations in Fig. 8 suggest that it is playing a significant role in fitting

to the data. Even more concerning in the BM results is the positive correlation inferred between K_0 and K'_0 since this is not physically realistic. While a closer look at the distribution in Fig. 8 reveals a bi-modal feature that artificially skews the correlation to positive, these concerns taken together are indicators the BM model may have relevant model form error for this application.

The NP BMC results in Fig. 9 are difficult to interpret without the corresponding baseline Sesame 3732 isentrope since the knot magnitudes represent the scaling of this curve. However, there are several features in the pair plot worth highlighting. First, the correlation between the knots is seen to be high between neighboring knots and gradually decreases as the knots become more separated. For example, the bivariate distribution of c_2 and c_3 near the center of Fig. 9 is extremely oblong showing high correlations, while moving to c_1 and c_5 on the bottom row shows a more circular uncorrelated distribution. Of course, this is the very nature of autocorrelation, but it illustrates that the calibration is correctly capturing this behavior. Second, and more importantly, the distributions reveal good inference of the parameters. The prior for the knots is a uniform distribution over a span of roughly 45%; therefore, a high degree of learning is taking place to constrain these knots to the 1% level. The exception is the inference of ρ_0 , which is rather broad and is bumping up against its physically imposed limits of roughly 3- σ of the prior. This is not entirely unexpected given the lack of sensitivity to ρ_0 for this model in Fig. 5, but it suggests errors could be further reduced by



15 December 2023 15:38:29

FIG. 9. Pair plot for BMC using the non-parametric model. The diagonals contain histograms of the 1D posterior distributions overlaid with a KDE of the distribution. The off-diagonal plots are the 2D marginal distributions and are represented by a KDE on the lower diagonals and points directly from the MCMC chain colored by the log likelihood on the upper diagonals. The axis ticks correspond to $\pm 2\sigma$ values.

introducing a more informative prior or removing it from the calibration entirely and then propagating the prior error through to the final results (i.e., to the pressure).

To evaluate the accuracy and precision of the calibrations, the results are compared to the traditional interpretation of these data through inverse Lagrangian analysis (ILA) presented in Paper I.¹ ILA is a well-accepted analysis methodology with rigorous uncertainty quantification and is, thus, believed to be the gold standard to which these calibrations should be compared. As a point of clarity, the principal isentrope is used as the reference curve for BMC, and therefore, the comparison is made to the reduced

isentrope from Ref. 1 and not the reduced room-temperature isotherm that is the focus of that work. This decision was made as the isentrope is believed to be most representative of these experiments, and it mitigates an extra step in the reductions that could cloud the comparisons. However, the calibration methods could easily be adapted to use an isotherm as the reference curve instead. Given the agreement of the calibrations with ILA that will be shown, we defer the reader to Paper I¹ if fits to the room-temperature isotherm are desired.

The calibration results are represented in the Eulerian sound speed-strain and pressure-strain spaces in Figs. 10 and 11,

respectively. These plots are the results of propagating the relevant posterior parameter distributions from BMC through the respective models to obtain these reference isentropes with well quantified uncertainties. Figure 10 represents the NP calibration space, while Fig. 11 is most representative of the parametric model form. Both figures contain subplots representing the $1-\sigma$ standard errors for each curve and the percent difference of the means from the ILA result as an attempt to best visualize differences in the uncertainty quantification, differences in the means, and, combined, if there are any quantifiable differences beyond the error bars.

In the sound speed space, we find excellent agreement in the uncertainties of all three calibrations and ILA (center panel of Fig. 10). The biggest discrepancy is at low strains where ILA contains significant uncertainties to strains of ~ 0.025 due to the velocity uncertainty being large with respect to the rate of change of velocity in this regime. Since correlations between the NP model knots result in inference over larger regions of velocity, this highly localized ILA behavior does not manifest in the BMC results. Beyond this difference, though, the errors are remarkably similar. The Vinet errors track almost exactly with the ILA results and gradually increase from 0.25% to 0.75%. The NP errors are similar, although they increase at a faster rate over the second half of the

compression to 1.5% due to the reduced sensitivities at the highest pressures, as elaborated on in the next paragraph. The BM uncertainties are the outlier, but not outrageously so, although the larger errors are another indicator of more difficulty in fitting to the data and the potential model form error.

A subtlety worth highlighting is the difference in the nature of the error profile between the NP BMC and ILA, where the NP result has a nonlinear upturn toward peak compression. This is believed to be a physically realistic feature since the wave reverberation creates a diminishing spatial region of high pressure within the sample. In other words, the impedance mismatch between the high-impedance Pt sample and the lower impedance LiF window creates wave interactions that result in significant portions of the sample that never reach the peak pressure. In fact, for a majority of the experiments, the region of peak pressure asymptotically approaches zero thickness. Thus, the effective sample thickness over which there is wave evolution at the highest velocities is markedly less than the actual sample thickness, and therefore, we hypothesize that the corresponding uncertainties in wave speed should also be higher. This feature is not captured in ILA because the characteristics approach maps to an *in situ* configuration where the window is effectively non-existent, and so, the entirety of the

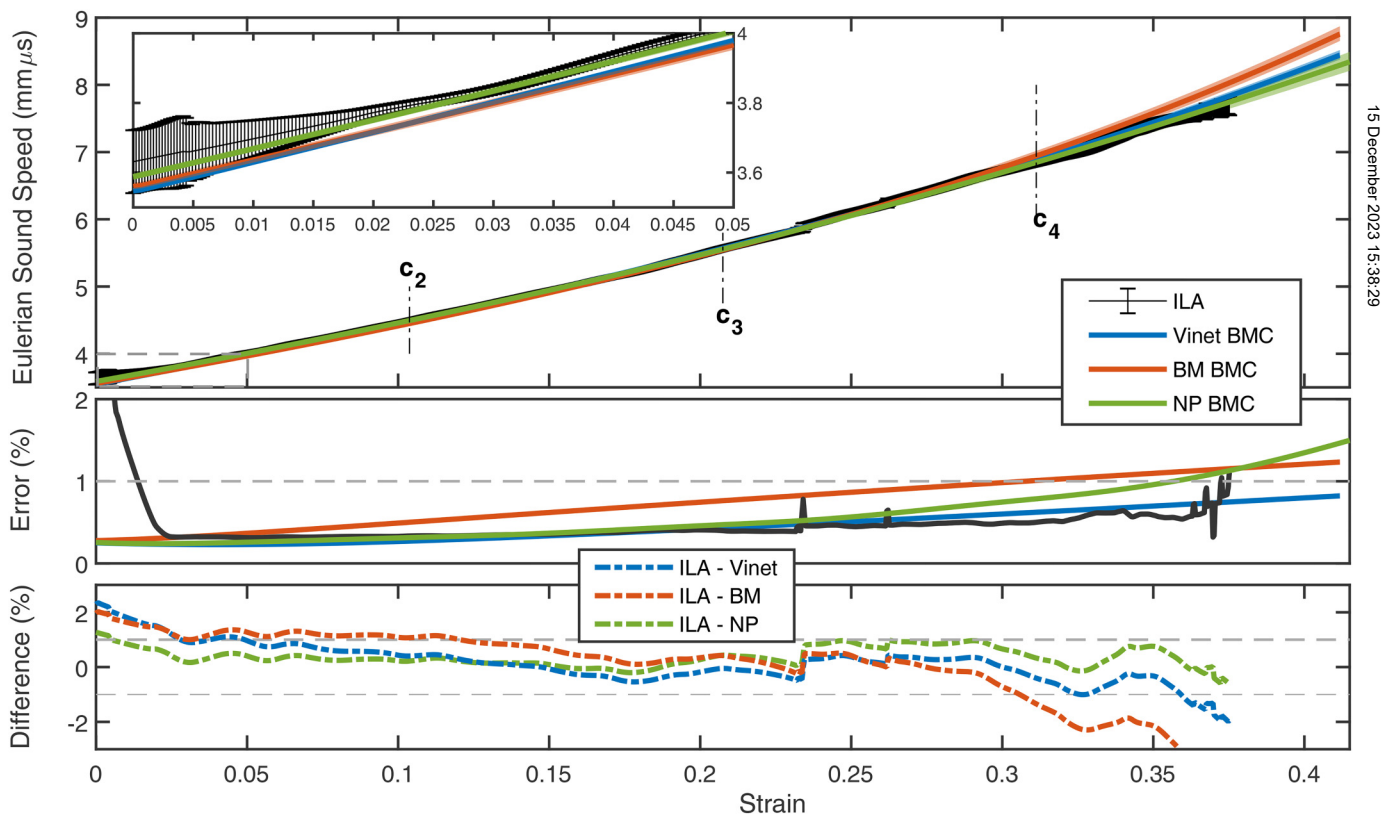


FIG. 10. Results of the BMC parametric and non-parametric calibrations compared to ILA in the sound speed–strain space. The top panel shows the magnitudes with $1-\sigma$ error bars on the ILA and 68% credible intervals as shaded regions on the BMC, with NP knot locations in strain indicated by c_2 – c_4 (c_1 and c_5 coinciding with the axis limits). The center panel shows the standard errors ($1-\sigma$) from all four results. The bottom panel is the percent difference in the mean of each BMC result from the ILA.

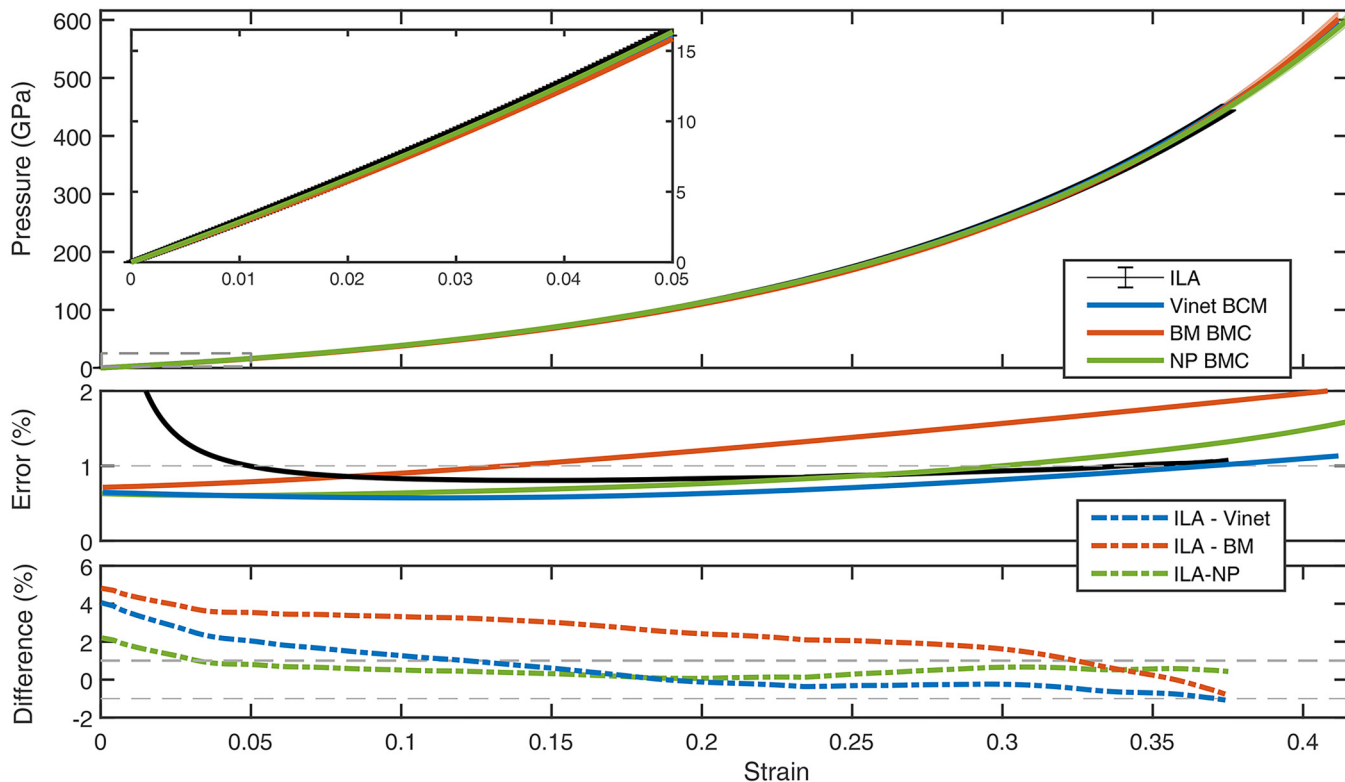


FIG. 11. Results of the BMC parametric and non-parametric calibrations compared to ILA in the pressure-strain space. The top panel shows the magnitudes with $1-\sigma$ error bars on the ILA and 68% credible intervals as shaded regions on the BMC. The center panel shows the standard errors ($1-\sigma$) from all four results. The bottom panel is the percent difference in the mean of each BMC result from the ILA.

15 December 2023 15:38:29

sample experiences the highest pressures. Conversely, this effect is naturally captured within the NP BMC because it is operating on simulations of the true experimental configuration. Translating to more quantitative terms, the pressure at the window interface is roughly three times less than the pressure on the driven side of the Pt due to the impedance mismatch, and therefore, pressures above 200 GPa should contain increased uncertainty. A pressure of 200 GPa corresponds to a strain of 0.27, which is where the NP and ILA errors begin to diverge. This point of divergence lends confidence to the hypothesis and further suggests that ILA could be underestimating the high pressure wave speed errors by close to a factor of 1.75. Moreover, since the parametric models are primarily constrained by the lower pressures and cannot capture this type of localized error behavior, this also suggests that the parametric BMC can underestimate the high-pressure uncertainty, albeit for a completely different reason than ILA.

The errors in the center panel of Fig. 10 compare favorably with the differences of the mean curves of the BMC and ILA shown in the lower panel. The NP difference is comparable to magnitude of the errors over the entirety of the curve except for the jog at a strain of 0.23, which results from the ILA transitioning between averages over different numbers of experiments.

Regardless, all differences are within a $2-\sigma$ overlap in the error bars, which suggests that there are no statistically meaningful differences between the results. The same is mostly true for the parametric results. The inset highlights the 1% differences at low strains, which is just on the edge of a $2-\sigma$ overlap. This difference tracks to the small offsets in the initial sound speed, where estimates of 3.548 ± 0.009 (Vinet), 3.560 ± 0.010 (BM), and 3.585 ± 0.009 (NP) are obtained. While these estimates compare well to within their uncertainties, they are systematically low (but still within the errors) compared to the prior value reported in Ref. 1 of 3.617 ± 0.055 . This systematic offset may suggest a tighter prior on K_0 or c_1 could marginally improve the respective calibrations. The more definitive difference is in the comparisons at strains above 0.35, particularly for the BM model. In this case, the differences go off scale and approach 4%, which is well outside of anticipated errors and further indication of a model form error. These discrepancies explain the lack of coverage in the high velocity regions in Fig. 6 where the higher wave speeds can result in earlier arrival times when compared to the data.

Comparisons in the pressure-strain space in Fig. 11 reveal similar trends. The ILA errors are higher at low strains but quickly drop to $\sim 0.8\%$ before rising slowly to 1%. The Vinet, BM, and NP

errors start at a slightly lower level of 0.7% before rising to 1.1%, 2%, and 1.6% respectively. These results largely follow the trends observed in the sound speed space, where Vinet is the lowest overall, NP has a higher rate of increase at higher strains, and BM is the largest. However, because of differences in how pressure is calculated, there are subtle differences in the overall error budgets. For the parametric models, pressure-strain is close to their native space [Eqs. (5) and (6)], and therefore, the errors come directly from the posterior distributions on ρ_0 , K_0 , and K'_0 . The NP and ILA errors, on the other hand, result from integration of the sound speed, and therefore, the error at a given pressure is a cumulative effect. The largest consequence of this integration is in the ILA's propagation of its low strain uncertainty. The result is higher overall errors in the ILA until the high-pressure NP non-linearity causes a crossover. Since there is some cancellation in these effects, the end result is less discrepancy in the pressure errors at peak strain as the NP result exceeds ILA by only a factor of 1.25.

While we highlighted some subtle differences in the nature of the uncertainties between the different methods, the overall differences between the calibrations and ILA largely fall within these errors. The Vinet and NP results are within the ILA errors, while BM is systematically low over much of the curve and just outside of a 2σ overlap of the error bars. Thus, like the results in sound speed space, there are some indications of problems with the BM model, but it is difficult to identify significant differences between the Vinet, NP, and ILA methods.

A final note with Fig. 11 is the peak pressure plotted of ~ 600 GPa. This contrasts with the peak experimental pressures only reaching 570 GPa and is the result of the final knot being a little too high since the form of the model makes *a priori* determination of the pressure difficult. Thus, the BMC result represents a small extrapolation and should technically be cutoff $\sim 2\%$ lower at a strain closer to 0.408 for any subsequent use of the data. Of course, the correlation between the knots still creates good sensitivity to the final knot despite it being beyond the range of the data. As such, this may result in a minor overestimation of the error, but it does not change the overall interpretation or comparisons to ILA, and therefore, we leave the full range in Figs. 10 and 11 as a reasonable representation of the calibration space with the caveat that they represent a slight extrapolation.

The overall conclusion from the comparison between BMC and ILA is the calibrations result in sufficient accuracy and precision to suggest that this is a viable analysis methodology for interpreting ramp compression experiments. The NP model, in particular, contains features in the error estimates believed to be physically realistic that are not captured by the parametric models or ILA. Moreover, it is difficult to identify any significant differences in the ILA and NP results to within their respective uncertainty estimates. The parametric model results are also reasonable despite indications that the BM model could be suffering from some model form error. The Vinet model appears to produce very good calibration and is an excellent representation of the ILA results. However, it would be difficult to know if either of the parametric results is valid in the absence of comparisons to the ILA or NP results, and therefore, we caution against generalizing this result to other scenarios.

IV. CONCLUSIONS

In this work, we examined feasibility and best practices associated with applying modern statistical methods to the interpretation of Pt shockless compression experiments performed on the Z machine. The methods recently developed by Francom *et al.*⁹ were found to be well-suited to our application where not only is the fully functional nature of the velocity-time histories accurately incorporated, but the alignment in both time and velocity enables high fidelity calibrations. The performance of these Bayesian calibrations was assessed through quantitative comparisons to inverse Lagrangian analysis, the traditional analytic analysis method for these types of data. We find that the overall accuracy and precision across a range of calibrations is similar to the traditional analysis. Thus, Bayesian calibration is found to be a viable approach to interpret and extract quantitative information from these high-pressure Pt shockless compression experiments.

The primary challenge in utilizing the Bayesian methods was in determining the model form describing the Pt isentrope. Our exploration of parametric models, such as Vinet and Birch-Murnaghan, identified potential issues, such as a lack of sensitivity over the entirety of the measurement, suggesting that these model forms are not highly constrained at the highest pressures. In practice, we found that the Vinet model provides excellent agreement with Lagrangian analysis over the full range of the data and is appropriate for this application, and therefore, Vinet results in Table III are a reasonable analytic representation of the isentrope extracted in this work. The Birch-Murnaghan model, on the other hand, results in apparent model form error and does not fit the data well at the highest pressures, and therefore, these calibration results are not recommended for further use. However, the success of the Vinet form is believed to stem from its ability to accurately represent the Pt compression response such that lower pressure constraints from the calibration extrapolate well over the range of the data. As such, we recommend the wider ranging fits of the ILA results in Paper I (Table IV of Ref. 1, which contains both the isentrope and isotherm) as the most appropriate parameter set for most applications.

Due to concerns about how well parametric model forms will generalize across a range of experimental platforms and materials, we also examined a novel non-parametric model (NP) form constructed to provide sensitivity over the entire range of the measurement. The NP construction consists of an arbitrary set of knots coupled with spline interpolation to generate the reference isentrope curve of interest. Sensitivity analysis suggests that this NP construction successfully produces sensitivities in the reference curve over the full range of the measured data. The compromise with the NP model form when compared to the parametric models is the introduction of auto-correlation between the knots, which ultimately results in a bias-variance trade-off where more knots results in lower bias at the cost of higher variance. However, we find optimization around this trade-off resulted in calibration in excellent agreement with both Lagrangian analysis and the Vinet calibration. Interestingly, we find that while the low-pressure NP errors are in excellent agreement, the higher pressure errors increase at a faster rate than any other analysis method. This is believed to be a realistic result stemming from wave interactions,

resulting in a significant decrease in the amount of sample material that reaches these higher pressures, an effect that the other methods do not capture. Thus, the NP approach is not only viable, but it may be preferable to not only guarantee that the results are constrained over the full range of the data, but also as a more realistic representation of the overall uncertainties. More generally, the performance of parametric models will likely not be known *a priori*, and therefore, NP calibrations are suggested as a useful diagnostic for unbiased comparisons. Furthermore, in scenarios where parametric model forms are found to be insufficient or altogether unknown, the NP approach offers a viable path forward. For example, the NP approach may provide a potential path toward analyzing data with obvious signatures of phase transitions, which generally result in a non-monotonic sound speed response.

ACKNOWLEDGMENTS

The authors would like to thank the large team of technicians and engineers at the Z machine involved in building and executing these experiments, several colleagues at Livermore National Laboratory for helpful discussions, and Marcus Knudson for reviewing the manuscript. Sandia National Laboratories is a multimission laboratory managed and operated by the National Technology & Engineering Solutions of Sandia, LLC, a wholly owned subsidiary of Honeywell International, Inc., for the U.S. Department of Energy's National Nuclear Security Administration under Contract No. DE-NA0003525. This paper describes objective technical results and analysis. Any subjective views or opinions that might be expressed in the paper do not necessarily represent the views of the U.S. Department of Energy or the United States Government.

AUTHOR DECLARATIONS

Conflict of Interest

The authors have no conflicts to disclose.

Author Contributions

Justin L. Brown: Conceptualization (equal); Formal analysis (lead); Investigation (equal); Methodology (equal); Writing – original draft (lead); Writing – review & editing (lead). **Jean-Paul Davis:** Conceptualization (equal); Data curation (lead); Formal analysis (equal); Investigation (equal); Methodology (equal); Writing – original draft (equal); Writing – review & editing (equal). **J. Derek Tucker:** Formal analysis (equal); Investigation (equal); Methodology (equal); Software (equal); Writing – original draft (equal); Writing – review & editing (equal). **Gabriel Huerta:** Formal analysis (equal); Investigation (equal); Methodology (equal); Software (equal); Writing – original draft (equal); Writing – review & editing (equal). **Kurtis W. Shuler:** Formal analysis (equal); Investigation (equal); Methodology (equal); Software (equal); Writing – original draft (equal); Writing – review & editing (equal).

DATA AVAILABILITY

The data that support the findings of this study are available from the corresponding author upon reasonable request.

APPENDIX A: MAGNETIC FIELD ERROR PARAMETERIZATION

Figure 11 in Paper 1¹ and the surrounding discussion details the impedance matching from the Cu electrode to the LiF window. This effectively describes the relationship between the measured window velocity u_{win} and the pressure in the copper electrode, P_{Cu} . Since the mechanical pressure in the copper is the direct result of the driving magnetic field, B , there is an equivalence between the mechanical and magnetic pressures such that

$$B(u_{\text{win}}) = \sqrt{2\mu_0 P_{\text{Cu}}(u_{\text{win}})}, \quad (\text{A1})$$

where μ_0 is the vacuum permeability constant. Uncertainty in the magnetic field can then be estimated through

$$\delta B = \frac{\partial B}{\partial u_{\text{win}}} \delta u_{\text{win}}. \quad (\text{A2})$$

Given the non-analytic nature of $P_{\text{Cu}}(u_{\text{win}})$, $\frac{\partial B}{\partial u_{\text{win}}}$ can be estimated numerically and combined with the known velocity uncertainty, Eq. (1), to solve for the magnetic field uncertainty. As a matter of convenience, the dependence of δB^2 on U_{con} and U_{lin} is kept separate such that their contributions can be isolated in the form

$$\delta B^2 = (\alpha U_{\text{con}})^2 + (\beta U_{\text{lin}})^2. \quad (\text{A3})$$

The α and β coefficients in Eq. (A3) can be calculated as a function of $B(u_{\text{win}})$ numerically, resulting in the curves in Fig. 12. In order to make practical use of these curves, analytic fits are required, for which we find that the power-law fits described in the legends accurately reproduce the numerical calculations. These fits are combined to give the final form for the magnetic field uncertainty used in this work as represented in Eq. (2).

15 December 2023 15:38:29

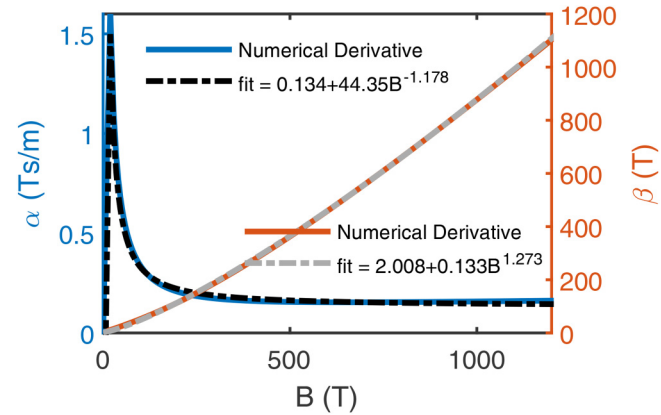
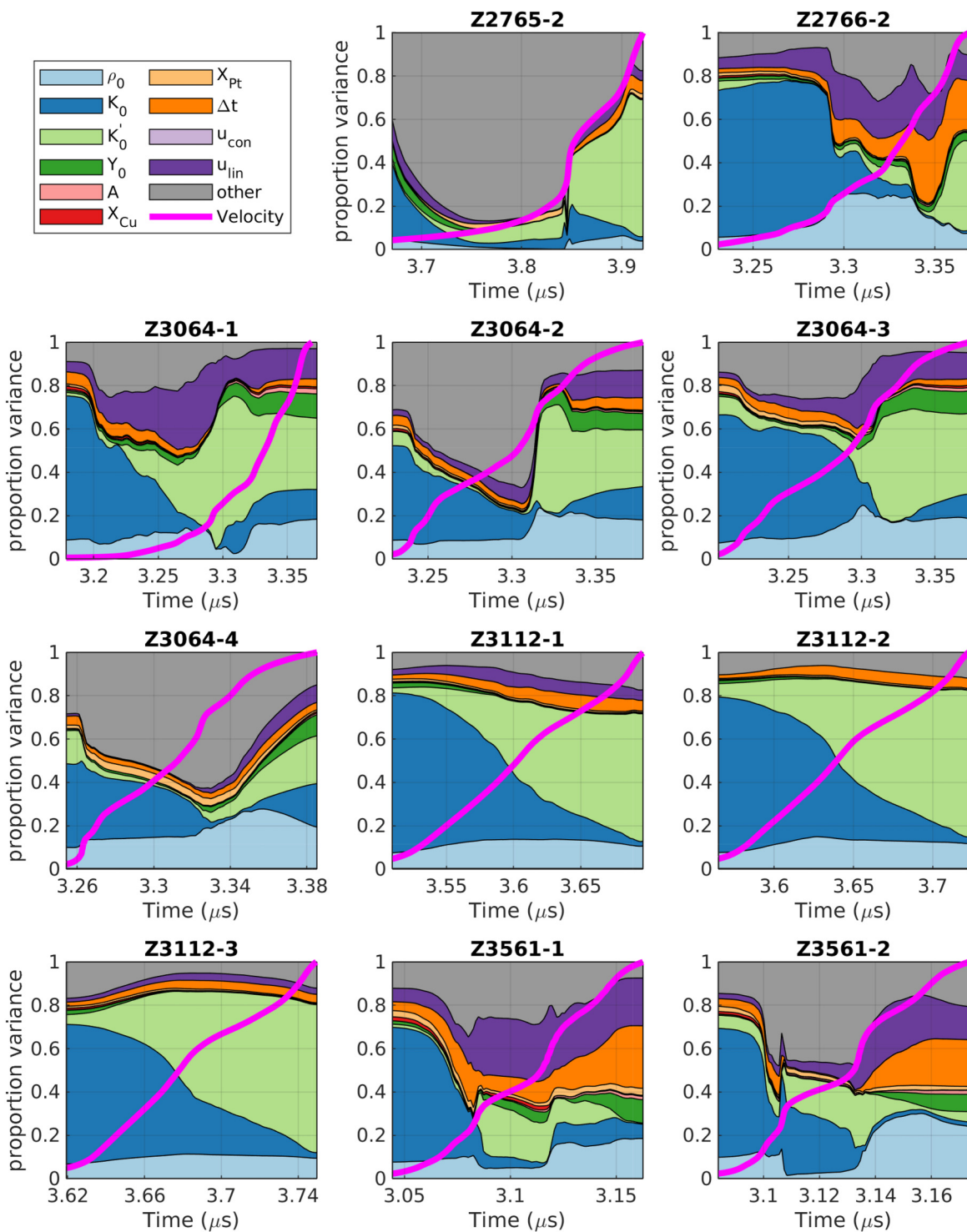


FIG. 12. Contributions to the magnetic field uncertainty as a function of the field magnitude. Power-law fits to each contribution give a good representation of the numerical derivatives.

APPENDIX B: COMPLETE SENSITIVITY ANALYSIS RESULTS



15 December 2023 15:38:29

FIG. 13. Sensitivity analysis for all the experiments using the Vinet model form and the posterior distributions from the corresponding BMC in Sec. III B. The proportion variance represents the first-order sensitivity index, and each parameter and experiment has a time-dependent structure related to the respective velocity profiles shown as the magenta curves.

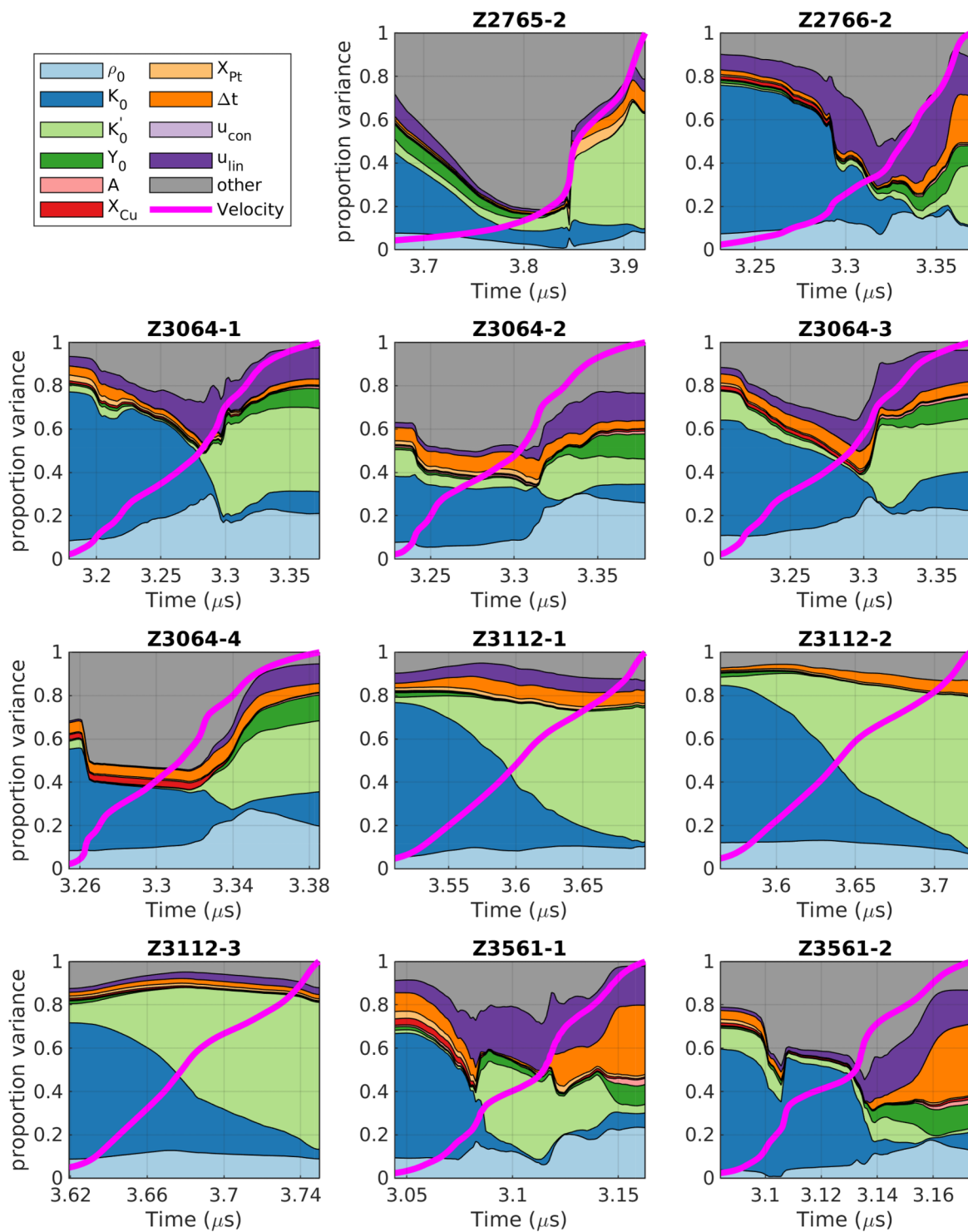
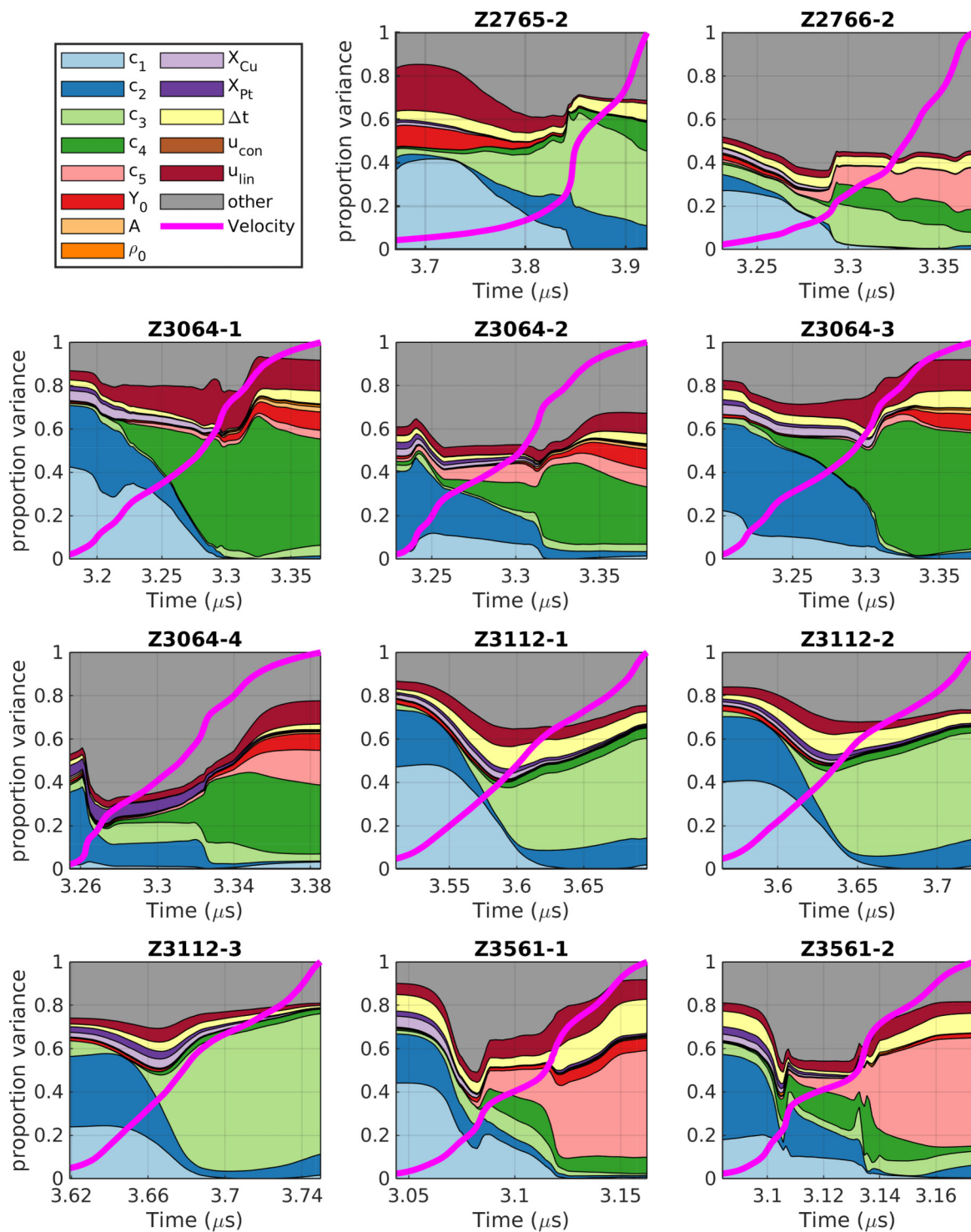


FIG. 14. Sensitivity analysis for all the experiments using the BM model form and the posterior distributions from the corresponding BMC in Sec. III B.

15 December 2023 15:38:29



15 December 2023 15:38:29

FIG. 15. Sensitivity analysis for all the experiments using the NP model form and the posterior distributions from the corresponding BMC in Sec. III B. The knot locations are shown in Fig. 10 where c_1 and c_5 correspond to the minimum (strain = 0) and maximum (strain = 0.415) of the axis.

REFERENCES

- ¹J.-P. Davis and J. L. Brown, "Quantifying uncertainty in analysis of shockless dynamic compression experiments on platinum. I. Inverse Lagrangian analysis," *J. Appl. Phys.* **134**, 235901 (2023).
- ²R. G. Kraus, J.-P. Davis, C. T. Seagle, D. E. Fratanduono, D. C. Swift, J. L. Brown, and J. H. Eggert, "Dynamic compression of copper to over 450 GPa: A high-pressure standard," *Phys. Rev. B* **93**, 134105 (2016).
- ³D. E. Fratanduono, M. Millot, D. G. Braun, S. J. Ali, A. Fernandez-Panella, C. T. Seagle, J. Davis, J. L. Brown, Y. Akahama, R. G. Kraus, M. C. Marshall, R. F. Smith, E. F. O'Bannon, J. M. McNaney, and J. H. Eggert, "Establishing gold and platinum standards to 1 terapascal using shockless compression," *Science* **372**, 1063–1068 (2021).
- ⁴R. W. Lemke, M. D. Knudson, D. E. Bliss, K. Cochrane, J. P. Davis, A. A. Giunta, H. C. Harjes, and S. A. Slutz, "Magnetically accelerated, ultrahigh velocity flyer plates for shock wave experiments," *J. Appl. Phys.* **98**, 073530 (2005).
- ⁵J.-P. Davis, J. L. Brown, M. D. Knudson, and R. W. Lemke, "Analysis of shockless dynamic compression data on solids to multi-megabar pressures: Application to tantalum," *J. Appl. Phys.* **116**, 204903 (2014).
- ⁶J. L. Brown, C. S. Alexander, J. R. Asay, T. J. Vogler, D. H. Dolan, and J. L. Belof, "Flow strength of tantalum under ramp compression to 250 GPa," *J. Appl. Phys.* **115**, 043530 (2014).
- ⁷M. C. Kennedy and A. O'Hagan, "Bayesian calibration of computer models," *J. R. Stat. Soc. Ser. B Stat. Methodol.* **63**, 425–464 (2001).
- ⁸J. L. Brown and L. B. Hund, "Estimating material properties under extreme conditions by using Bayesian model calibration with functional outputs," *J. R. Stat. Soc. Ser. C Appl. Stat.* **67**, 1023–1045 (2018).
- ⁹D. Francom, J. D. Tucker, G. Huerta, K. Shuler, and D. Ries, "Elastic Bayesian model calibration," *arXiv:2305.08834* (2023).
- ¹⁰J. Brynjarsdattir and A. O'Hagan, "Learning about physical parameters: The importance of model discrepancy," *Inverse Probl.* **30**, 114007 (2014).
- ¹¹R. F. Smith, J. H. Eggert, D. C. Swift, J. Wang, T. S. Duffy, D. G. Braun, R. E. Rudd, D. B. Reisman, J.-P. Davis, M. D. Knudson, and G. W. Collins, "Time-dependence of the alpha to epsilon phase transformation in iron," *J. Appl. Phys.* **114**, 223507 (2013).
- ¹²L. Barker and R. Hollenbach, "Laser interferometer for measuring high velocities of any reflecting surface," *J. Appl. Phys.* **43**, 4669–4675 (1972).
- ¹³J. Robbins, personal communication (2011).
- ¹⁴J. H. J. Niederhaus, S. W. Bova, J. B. Carleton, J. H. Carpenter, K. R. Cochrane, M. M. Crottat, W. Dong, T. J. Fuller, B. N. Granzow, D. A. Ibanez, S. R. Kennon, C. B. Luchini, R. J. Moral, C. J. O'Brien, M. J. Powell, A. C. Robinson, A. E. Rodriguez, J. J. Sanchez, W. A. Scott, C. M. Siefert, A. K. Stagg, I. K. Tezaur, T. E. Voth, and J. R. Wilkes, "ALEGRA: Finite element modeling for shock hydrodynamics and multiphysics," *Int. J. Impact Eng.* **180**, 104693 (2023).
- ¹⁵D. Dolan, "Foundations of VISAR analysis," *Sandia Report No. SAND2006-1950* (Sandia National Laboratories, 2006).
- ¹⁶J. L. Brown, J. P. Davis, and C. T. Seagle, "Multi-megabar dynamic strength measurements of Ta, Au, Pt, and Ir," *J. Dyn. Behav. Mater.* **7**, 196–206 (2021).
- ¹⁷D. J. Steinberg, S. G. Cochran, and M. W. Guinan, "A constitutive model for metals applicable at high-strain rate," *J. Appl. Phys.* **51**, 1498–1504 (1980).
- ¹⁸BMC uses Eq. (4), while ILA uses a power-law form with a coefficient of 0.94, but this is calculated to be a negligible difference.¹
- ¹⁹P. Vinet, J. Rose, J. Ferrante, and J. Smith, "Universal features of the equation of state of solids," *J. Phys.: Condens. Matter* **1**, 1941–1963 (1989).
- ²⁰F. Birch, "Finite elastic strain of cubic crystals," *Phys. Rev.* **71**, 809–824 (1947).
- ²¹F. N. Fritsch and R. E. Carlson, "Monotone piecewise cubic interpolation," *SIAM J. Numer. Anal.* **17**, 238–246 (1980).
- ²²I. M. Sobol', "Global sensitivity indices for nonlinear mathematical models and their Monte Carlo estimates," *Math. Comput. Simul.* **55**, 271–280 (2001).
- ²³D. Francom, B. Sanso, A. Kupresanin, and G. Johannesson, "Sensitivity analysis and emulation for functional data using Bayesian adaptive splines," *Stat. Sin.* **28**, 791 (2018).
- ²⁴The models are expressed as a function of strain, but an initial density is required to run the simulations.
- ²⁵C. W. Greeff, J. Brown, N. Velisavljevic, and P. A. Rigg, "Phase transitions in high-purity zirconium under dynamic compression," *Phys. Rev. B* **105**, 184102 (2022).
- ²⁶M. J. Bayarri, J. O. Berger, J. Cafeo, G. Garcia-Donato, F. Liu, J. Palomo, R. J. Parthasarathy, R. Paulo, J. Sacks, and D. Walsh, "Computer model validation with functional output," *Ann. Stat.* **35**, 1874–1906 (2007).
- ²⁷D. Francom, B. Sanso, V. Bulaevskaya, D. Lucas, and M. Simpson, "Inferring atmospheric release characteristics in a large computer experiment using Bayesian adaptive splines," *J. Am. Stat. Assoc.* **114**, 1450–1465 (2019).
- ²⁸D. Higdon, J. Gattiker, B. Williams, and M. Rightley, "Computer model calibration using high-dimensional output," *J. Am. Stat. Assoc.* **103**, 570–583 (2008).
- ²⁹J. D. Tucker, W. Wu, and A. Srivastava, "Generative models for functional data using phase and amplitude separation," *Comput. Stat. Data Anal.* **61**, 50–66 (2013).
- ³⁰A. Srivastava and E. Klassen, *Functional and Shape Data Analysis* (Springer, 2016).
- ³¹A. Gleman, J. B. Carlin, H. Sern, D. Duson, A. Vehtari, and D. Rubin, *Bayesian Data Analysis*, 3rd ed. (Chapman & Hall/CRC, 2013).
- ³²K. R. Cochrane, P. Kalita, J. L. Brown, C. A. McCoy, J. W. Gluth, H. L. Hanshaw, E. Scoglietti, M. D. Knudson, S. P. Rudin, and S. D. Crockett, "Platinum equation of state to greater than two terapascals: Experimental data and analytical models," *Phys. Rev. B* **105**, 224109 (2022).

15 December 2023 15:38:29